separations

Review

Converting Industrial Inorganic Solid Wastes from Chemical Processes into High-Efficiency Adsorbents: A Review

Ruiling Du [1,2], Xiaoya Li [1,2] and Shuai Wang [1,2,*]

[1] College of Chemistry and Chemical Engineering, Central South University, Changsha 410083, China
[2] Hunan Provincial Key Laboratory of Efficient and Clean Utilization of Manganese Resources, Central South University, Changsha 410083, China
* Correspondence: wangshuai@csu.edu.cn

Abstract

With ongoing development in the process industries, the accumulation of industrial inorganic solid wastes (IISWs) has become increasingly significant. IISWs are characterized by large volume and toxicity and pose challenges in treatment and control. IISWs from chemical processes mainly include red mud (RM), zinc slag, lithium slag (LS), electrolytic manganese residue (EMR), phosphogypsum (PG), water treatment sludge (WTS), sewage sludge, blast furnace slag (BFS), steel slag (SS), coal fly ash (CFA), coal gasification slag (CGS), copper smelting slag (CSS), and lead smelting slag (LSS). Having been chemically processed, they exhibit complex compositions that pose challenges for further utilization. In this paper, we comprehensively review the preparation of adsorbents from IISWs as raw materials, the applications of IISW-derived adsorbents, and their adsorption mechanisms. The obtained adsorbents include modified IISWs, zeolites, porous ceramics, and composite and hybrid adsorbents. The adsorption mechanisms, such as van der Waals forces, electrostatic interactions, and π–π interactions, contribute to the rapid adsorption kinetics and high adsorption capacity observed in these adsorbents.

Keywords: inorganic solid waste; adsorbent; preparation; adsorption; mechanism

1. Introduction

With the rapid development of modern industrial chemical processes such as metallurgy, chemical engineering, and electronics manufacturing, massive amounts of industrial inorganic solid wastes (IISWs) are generated. Untreated IISWs not only occupy valuable land resources but also enter the atmosphere, water bodies, and soil through wind and water erosion, causing air pollution, water eutrophication, and heavy metal contamination. The improper stacking and disposal of IISWs has thus become a pressing environmental challenge, posing severe threats to ecological balance and human health. In this context, exploring sustainable utilization pathways for IISWs has emerged as a critical focus in environmental protection and resource recycling [1].

The treatment technologies for IISWs primarily encompass two strategic approaches: eliminating or converting harmful substances within them into non-hazardous forms, and extracting valuable components or transforming them into various high-value products. Given the substantial production volume of IISWs, their resource utilization represents an optimized strategy for supporting the development of related industries and protecting the ecological environment. Among the various resourceization strategies, utilizing IISWs to prepare adsorption materials stands out as a win–win approach that achieves both waste

Check for updates

Academic Editor: Guojie Zhang

Received: 10 January 2026
Revised: 20 February 2026
Accepted: 24 February 2026
Published: 3 March 2026

Copyright: © 2026 by the authors. Licensee MDPI, Basel, Switzerland. This article is an open access article distributed under the terms and conditions of the Creative Commons Attribution (CC BY) license.

reduction and resource reclamation. Compared to commercial adsorbents, adsorbents derived from IISWs offer inherent advantages of cost-effectiveness and accessibility, as they leverage underutilized waste streams while minimizing raw material costs [2]. Moreover, this strategy aligns with environmental sustainability goals by extending waste lifecycles, reducing disposal burdens, and addressing pollution from dual perspectives—waste management and pollutant treatment. However, due to the wide variety and diverse properties of IISWs, systematic summarization remains necessary to provide a reference for the preparation and application of adsorbents from these wastes.

On the other hand, the growing demand for adsorbents in environmental applications, including wastewater treatment, exhaust gas purification, and soil remediation, underscores the need for sustainable and cost-effective materials. In wastewater treatment, various technologies have been developed, including coagulation, sedimentation, flotation, filtration, ion exchange, membrane processes, adsorption, and chemical precipitation. Among these methods, adsorption is considered particularly suitable for wastewater treatment due to its convenience, simple operation, and straightforward design [3]. Additionally, adsorption can be used for metal ion separation and for the treatment of low-concentration solutions. In rare earth separation, it is currently the most effective approach, capable of separating all rare earth elements (REEs) [4]. In exhaust gas treatment, adsorption and absorption are among the most effective technologies, and adsorbents and absorbents are critical to process efficiency, operational cycles, and treatment costs [5]. In soil remediation, adsorbents can serve as key soil amendments. These materials function by adsorbing or immobilizing harmful substances, such as heavy metals, making them essential agents in remediation technologies [6]. Therefore, wastewater treatment, exhaust gas purification, and soil remediation all rely on adsorbents and their associated adsorption technologies. The core of adsorption technology lies in the performance of adsorbents. Yet, the high cost of conventional adsorbents—such as ion exchange and adsorption resins [7], graphene-based adsorbents [8], and zeolites [5]—often limits their large-scale application. Efforts have been spurred to develop low-cost alternatives, with IISWs emerging as promising precursors due to their abundant reserves, diverse compositions, and potential for functional modification. To contextualize the potential of IISWs in these fields, it is essential to understand the role of adsorption in established separation processes.

This paper comprehensively explores the preparation methods, application scenarios, and adsorption mechanisms of adsorbents derived from IISWs. By systematically synthesizing existing research and technical practices, it aims to provide a reference for the high-value utilization of IISWs and offer insights for the development of efficient, low-cost adsorbents—both of which are conducive to advancing environmental remediation and promoting sustainable development.

2. Classification, Properties, and Treatment Technologies of IISWs

2.1. Classification and Generation

2.1.1. Classification

Industrial chemical processes frequently involve hydroprocessing and high-temperature operations, which generate substantial IISWs [9]. According to their process characteristics, IISWs are classified into two categories: those derived from hydroprocesses and those from high-temperature processes. IISWs from hydroprocesses are characterized by a wide variety of hazardous elements, fine particle sizes, and often contain water, soluble salts, and various metal elements. The components of IISWs from high-temperature processes are relatively complex, containing various insoluble phases and soluble salts.

https://doi.org/10.3390/separations13030083

2.1.2. Generation of IISWs in Hydroprocesses

IISWs from hydroprocesses are commonly generated during leaching [10], precipitation, sedimentation, and filtration processes in hydrometallurgy, solid waste management, and wastewater treatment. They typically include non-ferrous hydrometallurgical residues, electrolytic manganese residue (EMR), phosphogypsum (PG), water treatment sludge (WTS), and sewage sludge. The non-ferrous hydrometallurgical residues mainly consist of red mud (RM), zinc leaching residue (ZLR), and lithium slag (LS).

Bauxite residue, commonly known as red mud, is a highly alkaline solid waste generated during alumina production in the Bayer process, sintering process, and combination methods. Red mud from the Bayer process is a hydrometallurgical residue, while that from the sintering process is a residue of high-temperature roasting followed by leaching. Red mud is also generated during the combination process. Approximately 1–2 tons of red mud are produced per ton of alumina. With the sustained growth of the global aluminum industry, annual red mud production has reached around 180 million tons. It continues to rise annually, while global reserves exceed 4 billion tons [11]. Notably, as high-quality bauxite resources dwindle, aluminum producers are increasingly turning to low-grade bauxite, further exacerbating red mud production. Currently, the majority of red mud worldwide is stored in open-air impoundments or tailings ponds using wet stacking methods. Due to its high pH (typically 10–13) and high levels of sodium, aluminum, iron, and titanium, as well as trace amounts of metals (such as chromium, vanadium, and arsenic), long-term landfilling of red mud not only occupies vast land areas but also poses significant environmental risks. Under natural processes such as weathering and rainwater leaching, alkaline substances and hazardous elements from red mud may infiltrate groundwater or surface water, leading to water pollution, soil salinization, and ecosystem degradation. Moreover, dried red mud can easily generate dust, which may become airborne and pose a potential health threat to nearby populations [12].

Zinc slag, also known as zinc smelting slag, includes ZLR from zinc hydrometallurgy, zinc pyrometallurgical slag, neutralization residue from zinc-containing acidic wastewater in smelters, and so on. This slag has accumulated to over 10 million tons globally and continues to grow by approximately 320,000 tons annually [13]. The hydrometallurgical process is the main method of zinc smelting worldwide, accounting for more than 85% of zinc production [14]. As a result, ZLR is among the most prevalent forms of zinc slag. Approximately 0.96 tons of ZLR are generated per ton of zinc produced, resulting in an annual output exceeding 270,000 tons.

Lithium slag is the residue generated from lithium extraction using lithium ores or from salt lake lithium extraction, among which lithium leaching residue (LLR) is relatively common. Reports indicate that producing 1 ton of lithium carbonate generates 8–10 tons of lithium slag, while producing 1 ton of lithium hydroxide produces 20–40 tons of lithium slag. In 2021, China's lithium carbonate production was 215,900 tons, and lithium slag exceeded 2 million tons [15].

EMR is a solid waste generated during the production of electrolytic manganese. Typically, 7–10 tons of EMR are produced for every ton of electrolytic manganese. Currently, China's annual EMR output is approximately 11 million tons, accounting for over 98% of global production [16].

Phosphogypsum is an industrial waste produced during the hydroprocess of phosphoric acid production, which involves the reaction of phosphate rock with sulfuric acid. Approximately 4–5 tons of phosphogypsum are generated for every ton of phosphoric acid produced. According to statistics, the global annual production of phosphogypsum exceeds 280 million tons, with China producing 75 million tons annually, and total reserves exceed 600 million tons [17].

The water and wastewater treatment industries continue to expand in scale, generating substantial amounts of sludges during the processes. These types of sludges are characterized by complex composition and are rich in microorganisms, organic matter, heavy metals, and various suspended impurities. Although wastewater treatment is a category of water treatment, practical water treatment primarily focuses on treating water from sources, including surface water, river water, and groundwater, to produce qualified water for industrial, agricultural, and daily domestic use. WTS refers to solid waste generated during water treatment processes, including coagulation, flocculation, sedimentation, filtration, ion exchange and adsorption, and chemical precipitation. In the treatment processes, aluminum or iron salts, with less lime (calcium oxide), are used. These substances can be hydrolyzed to produce flocculating compounds with high specific surface area and porosity, enabling rapid, efficient adsorption of various impurities. Approximately 10,000 tons of dry WTS are produced worldwide daily, making WTS the largest residue generated by the water industry [18]. Unlike water treatment, wastewater treatment focuses on treating wastewater from domestic, industrial, and agricultural activities. Wastewater treatment processes may include procedures similar to the aforementioned water treatment processes. Still, they may also involve additional steps such as solvent extraction and membrane separation, depending on the nature of the wastewater and the treatment standards. Sewage sludge is produced during wastewater treatment. Since sludge is generated from various industries, its quantity is difficult to estimate.

2.1.3. Generation of IISWs in High-Temperature Processes

IISWs are generally generated during high-temperature processes such as pyrometallurgy, combustion, and gasification. They mainly include blast furnace slag (BFS), steel slag (SS), coal fly ash (CFA), coal gasification slag (CGS), copper smelting slag (CSS), and lead smelting slag (LSS). Although red mud from the sintering process undergoes a high-temperature process, it also undergoes hydroprocessing, as discussed in Section 2.1.2.

BFS is a non-metallic by-product generated during the iron-making process in a blast furnace, formed at high temperatures through reactions among gangue minerals in iron ore, coke ash, and added flux (primarily limestone, $CaCO_3$). It is estimated that 290 kg of BFS are produced for every ton of iron manufactured. In China, a large amount of BFS is currently disposed of in landfills, and 20% of it remains underutilized [19]. Landfilling BFS has led to serious contamination of groundwater with heavy metals and particulate matter. Proper treatment and resource recovery of BFS can not only reduce environmental pollution but also generate significant economic and social benefits.

Steel slag is an important by-product of the steel industry, with the highest production volume worldwide. China's production in 2021 exceeded 120 million tons, and it has accumulated over 1 billion tons of steel slag, yet its utilization rate is only about 20% [20]. Steel slag is characterized by wear resistance, uniform particle shape, and high porosity [21]. Most steel slag cannot be utilized promptly, leading to its burial or open-air storage, which consumes vast amounts of land. Moreover, because it contains various heavy metals, steel slag may seep into soil and waterways, posing threats to both the ecological environment and human health. Furthermore, the improper handling or transportation of steel slag during open-air storage or processing can generate significant dust, severely endangering atmospheric quality and public health.

CFA and CGS are by-products of coal combustion and gasification processes, respectively. Over 40% of global electricity production relies on coal, with an annual CFA generation of approximately 780 million tons. The concentration of heavy metals in CFA can sometimes be up to 10 times higher than that in raw coal; therefore, it is classified as hazardous waste [22]. CGS is produced with an annual emission exceeding 70 million tons.

This slag poses significant hazards, including land occupation and soil pollution, with its stockpile increasing at a rate of 4.8 to 5.29 million tons per year [23].

CSS and LSS are mainly produced during the pyrometallurgical smelting of copper and lead, respectively. It is estimated that for every ton of copper produced, about 2–3 tons of CSS are generated during smelting. Annually, approximately 68.7 million tons of CSS are discharged into the environment globally, with China accounting for 20.25 million tons [24]. The generation of LSS is also considerable, with millions of tons generated globally each year [25]. The widely used lead smelting process in China can produce approximately 7100 tons of LSS for every 10,000 tons of lead smelted [26].

2.1.4. Summary of Industrial Sources of IISWs

In summary, IISWs primarily originate from hydrometallurgical and high-temperature processes within the metallurgical, chemical engineering, energy, environmental, and water treatment industries, as summarized in Table 1.

Table 1. Classification and sources of industrial inorganic solid wastes (IISWs).

Classification	Industrial Sources			
	Metallurgy	Chemical Engineering	Energy	Water/Wastewater Treatment
IISWs from hydroprocesses	Red mud, ZLR, lithium slag, and EMR	Phosphogypsum		WTS and sewage sludge
IISWs from high-temperature processes	BFS, steel slag, CSS, LSS, and zinc pyrometallurgical slag	CGS	CFA	

2.2. Composition and Physicochemical Properties

2.2.1. General Chemical Composition

The composition of IISWs is often similar, with possible variations in elemental content. Elemental analysis and X-ray fluorescence spectrometry (XRF) detection of IISWs can determine their primary elemental composition. The main components of IISWs are sodium (Na), silicon (Si), aluminum (Al), magnesium (Mg), potassium (K), calcium (Ca), manganese (Mn), iron (Fe), titanium (Ti), etc. The composition reported in the literature is shown in Table 2. As can be seen from the table, most of these wastes contain significant amounts of elements such as Si, Al, Ca, and Fe, which often serve as active components in adsorbents. Elements like Na, Mg, K, and Ti are present in relatively lower amounts, and certain phases of these elements can also function as constituents of adsorbents. The data reveal considerable variation even within the same waste category. For example, red mud samples show silica (SiO_2) content ranging from 7% to 24%, and alumina (Al_2O_3) content from 19% to 26%. The data highlight that the specific industrial process, raw materials, and operational conditions greatly influence the final waste composition.

Table 2. Main chemical composition of IISWs.

IISWs	Composition (wt%)									Ref.
	Na_2O	SiO_2	Al_2O_3	MgO	K_2O	CaO	MnO [a] /MnO_2 [b]	Fe_2O_3 [c] /FeO [d]	TiO_2	
Red mud	13.76	23.82	25.28	/	0.77	13.76	/	17.21 [c]	3.04	[6]
	5.38	7.57	25.47	/	/	1.24	/	52.59 [c]	5.91	[27]
	9.95	16.88	19.79	/	/	19.05	/	20.92 [c]	9.06	[28]
ZLR	0.20	18.78	2.30	0.67	0.72	17.38	/	8.31 [c]	/	[14]

Table 2. *Cont.*

IISWs	Composition (wt%)									Ref.
	Na_2O	SiO_2	Al_2O_3	MgO	K_2O	CaO	MnO [a] /MnO_2 [b]	Fe_2O_3 [c] /FeO [d]	TiO_2	
Lithium slag	0.12	70.42	28.40	0.05	0.13	0.11	/	0.24 [c]	/	[15]
	0.33	53.22	17.11	0.41	0.53	10.11	/	1.48 [c]	/	[29]
	0.13	70.67	27.24	0.16	0.22	0.29	/	0.52 [c]	/	[30]
EMR	2.7	24.6	12.2	1.7	2.4	8.6	4.6 [a]	7.9 [c]	0.4	[31]
	/	26.64	10.18	1.56	1.94	20.31	2.93 [a]	5.72 [c]	/	[32]
	/	37.47	10.87	/	2.85	14.87	3.31 [a]	6.11 [c]	/	[33]
Phosphogypsum	0.22	5.32	0.28	/	0.24	26.6	/	0.2 [c]	/	[17]
	/	1.18	0.12	0.15	/	47.84	/	/	/	[34]
	/	6.68	0.38	/	/	30.08	/	/	/	[35]
WTS	0.04	40.33	31.84	0.48	1.32	0.09	/	6.43 [c]	0.46	[36]
	0.07	9.41	51.01	0.22	0.20	1.31	0.49 [a]	0.7 [c]	0.05	[37]
	0.3	54.1	28.84	0.64	0.75	3.1	0.37 [a]	9.92 [c]	1.28	[38]
BFS	0.27	29.13	20.59	1.11	/	47.08	/	1.58 [c]	/	[19,39]
	1.84	37.48	12.86	2.45	0.71	36.7	6.24 [a]	0.40 [c]	0.72	[38]
	0.7	41.1	8.2	3.12	0.3	37.2	2.64 [a]	2.51 [c]	/	[40]
Steel slag	/	13.50	2.31	5.80	/	45.50	2.24 [a]	24.30 [c]	/	[20]
	0.05	14.38	5.48	3.42	0.04	44.83	1.94 [a]	21.65 [c]	0.57	[21]
	/	12.33	0.18	10	/	32.73	3.29 [a]	38.83 [c]	/	[41]
CFA	0.11	48.97	40.26	0.4	0.49	2.29	0.02 [a]	3.07 [c]	1.52	[22]
	0.45	48.21	33.18	0.75	/	5.68	/	4.80 [c]	/	[42]
	5.15	48.09	18.48	3.96	/	10.36	0.14 [a]	8.40 [c]	0.94	[43]
CGS	1.73	58.45	24.36	0.96	3.12	2.35	/	4.70 [c]	1.95	[23]
	0.91	26.30	14.54	0.49	1.03	4.66	/	2.59 [c]	0.67	[44]
	0.94	51.34	26.66	1.18	1.59	12.28	/	4.24 [c]	1.10	[44]
CSS	3.2	42.7	22.1	1.4	1.2	10.6	0.2 [b]	12.1 [c]	1.0	[45]
	/	49.01	19.28	3.92	/	18.83	/	6.02 [d]	/	[46]
LSS	4.68	19.68	3.99	1.68	0.86	10.07	1.11 [a]	33.57 [c]	0.25	[25]

/, not reported; [a] MnO, [b] MnO_2, [c] Fe_2O_3, and [d] FeO.

2.2.2. Physicochemical Properties

IISWs generated during hydroprocesses typically contain water and soluble metal ions at specific concentrations, which constitute the primary environmental hazard. For instance, red mud mainly comprises iron, aluminum, titanium, silicon, calcium oxide, and various hydroxides, including hematite (Fe_2O_3), goethite (FeOOH), magnetite (Fe_3O_4), boehmite (γ-AlOOH), gibbsite ($Al(OH)_3$), anatase (TiO_2), rutile (TiO_2), quartz (SiO_2), calcite ($CaCO_3$), and perovskite ($CaTiO_3$). With pH typically ranging from 10 to 13, its high alkalinity poses a corrosive risk to the environment [47]. Zinc slag has a complex composition, rich in calcium, silicon, and iron elements. The primary mineral components are quartz (SiO_2), with small amounts of kyanite (Al_2SiO_5) and hematite (Fe_2O_3) also present [48]. The main components of lithium slag are silicon dioxide, aluminum oxide, calcium oxide, etc., and it may contain small amounts of lithium, potassium, sodium, and other alkali metal oxides. EMR primarily consists of quartz and gypsum dihydrate, containing high concentrations of Mn^{2+} and NH_4^+ ions with significant leaching toxicity. It also contains high concentrations of heavy metals, including manganese, cobalt, nickel, and lead. Phosphogypsum is a high-grade gypsum resource with a $CaSO_4 \cdot 2H_2O$ content exceeding 90%. It also contains other substances, such as soluble phosphorus pentoxide, soluble fluoride, co-crystalline phosphorus pentoxide, organic matter, and alkali metal salts [17]. The content and characteristics of WTS vary by location and depend on several factors, such as seasonal changes in raw-water quality, treatment processes, and chemical reagents. Chemically, the sludge consists mainly of silica, alumina, iron(III) oxide, and lime, along with trace amounts of heavy metals [49].

The high-temperature process generally involves material phase transformation, and the resulting IISWs have stable structures. BFS, composed of oxides such as CaO, Al_2O_3, and SiO_2, is traditionally used in construction and landfills due to its high strength and bulk density. The main chemical components of steel slag are SiO_2, Al_2O_3, CaO, and MgO [50]. CFA contains metal oxides, primarily SiO_2 and Al_2O_3, which are similar to the tetrahedrally positioned Si and Al in the framework structures of zeolite and kaolinite. Silicon can be sustainably recovered from CFA in the form of nanoparticles or aqueous solutions for the synthesis of zeolites. CGS consists of inorganic minerals and residual carbon particles, categorized into coarse and fine slag. The particle sizes of coarse slag are primarily within the 16–4 mesh range (1.19–4.75 mm), while fine slag falls below 200 mesh (0.075 mm). Coarse slag contains 5–30% residual carbon, whereas fine slag has 30–50% residual carbon, accounting for approximately 20% of total production. This slag contains incompletely burned residual carbon and exhibits abundant specific surface area and metal oxide minerals formed during high-temperature quenching. CSS contains various metals such as zinc, copper, and lead, and exhibits ultrafine particle size. LSS possesses volcanic ash activity. The slag contains various heavy metals, including Zn, Pb, Cd, As, and Cr. These heavy metals rarely occur in sulfides but are instead present in oxides, which are generally more soluble in the environment than sulfides [25].

2.3. Treatment Technologies

The key issues in industrial solid waste disposal include: how to mitigate its safety and environmental impact risks, how to further extract its valuable components, and how to achieve its resource utilization. Consequently, technologies for treating IISWs primarily include release back into the natural environment, stabilization and/or solidification, recovery of valuable elements, and production of various materials.

2.3.1. Release Back into the Natural Environment

The volumes of IISWs are extremely large. Therefore, the most commonly used strategy for their disposal at present is to release them back into the natural environment. The methods include landfilling, backfilling, and soilization, which release IISWs into landfills, goaf areas, and soil, respectively.

(1) Landfilling

Currently, the simplest method for solid waste disposal is landfilling, which is often the most economical option. However, landfilling typically requires substantial land resources and poses significant safety and environmental risks. IISWs containing no soluble salts or ammonia nitrogen pose relatively lower environmental risks during storage. In contrast, IISWs from hydroprocesses and fly ash often contain soluble salts, ammonia nitrogen, and heavy metals, thereby posing greater environmental risks. Therefore, such IISWs must undergo treatment to meet regulatory standards before landfilling. In China, the common practice is to collect EMR at open sites near factories. Still, these collection points are often poorly managed and fail to prevent their infiltration into the soil and surrounding areas. Since EMR contains some heavy metal elements and compounds, untreated discharge can cause severe pollution of the surrounding soil and receiving water bodies. Additionally, these collection sites occupy a large amount of land resources. For a long time, large-scale industrial activities that produce large amounts of EMR have been regarded as a burden due to the high costs of subsequent treatment and landfilling [51].

(2) Backfilling

Using IISWs for backfilling is widely regarded as an effective strategy for solid waste disposal. There are generally two methods of backfilling. One is to backfill IISWs during

the backfilling mining process. This method not only facilitates the disposal of IISWs but also enhances mining recovery and safety. Another method involves filling IISWs into existing goaf areas. The primary objective of this approach is to dispose of IISWs while providing some support to the goaf areas. Yao et al. [52] prepared coal-based cemented backfill material (CCBM) using CFA, coal gangue, and other coal-based solid wastes as primary raw materials, with a small amount of cement as binder and quicklime as an additive. This approach effectively reduces the accumulation and emission of IISWs. More importantly, backfilling significantly decreases the space for overburden movement. Yin et al. [53] utilized raw phosphogypsum as a filler. A composite binder was prepared by mixing CFA, yellow phosphorus slag (YPS), steel slag, and Portland cement. These four types of IISWs were incorporated into the cement paste backfilling (CPB) technique. After 60 days of curing, the unconfined compressive strength of the material ranged from 3.1 MPa to 19.5 MPa, providing a highly strengthened support to the mine to be filled with CPB.

(3) Soilization

Soil-based utilization of solid waste is a critical pathway to address pollution from waste stockpiling and achieve resource recycling. Modifying and regulating the physicochemical properties and aggregate structure of solid waste facilitates its transformation into a soil-like matrix, thereby supporting ecological restoration and sustainable utilization. Zhu et al. [54] investigated the stability of bauxite residue during the soil-formation process. By adding desulfurization gypsum and maize straw-Penicillium oxalicum, the alkalinity of bauxite residue was reduced. The pH decreased from an initial strong alkaline level (~10.5) to near neutrality (7.52), a reduction of approximately 3.0 units. The exchangeable sodium percentage (ESP) dropped from a high level (>50%) to 35.84%, effectively mitigating salinity hazards. Tang et al. [55] processed red mud to reduce its alkalinity, thereby enhancing nutrient availability and enzyme activity, which facilitates its pivotal role in driving carbon, nitrogen, and phosphorus cycles. In recent years, the soil improvement and soil chemicalization of phosphogypsum have become a research hotspot. Bossolani et al. [56] improved soil structure, increased soil organic matter content, and enhanced crop yields using phosphogypsum. Liu et al. [57] prepared three types of artificial soils using red mud and phosphogypsum. The study demonstrated that these artificial soils have the potential to support various bacterial-dominated biochemical reactions, thereby significantly enriching nutrient cycling and energy flow processes and enhancing their fertility and soil biological activity.

2.3.2. Stabilization and/or Solidification

Stabilization/solidification technologies can reduce the harm caused by heavy metal ions in IISWs by converting them into insoluble or non-migrating forms. Shu et al. [58] utilized MgO and phosphorus resources to simultaneously stabilize and solidify Mn^{2+} and NH_4^+-N in EMR. The efficiency of simultaneous stabilization and solidification for Mn^{2+} and NH_4^+-N reached 91.58% and 99.98%, respectively. Mn^{2+} was primarily stabilized in the forms of $Mn(H_2PO_4)_2{\cdot}2H_2O$, $Mn_3(PO_4)_2{\cdot}3H_2O$, $Mn(OH)_2$, and MnOOH, while NH_4^+-N existed as $NH_4MgPO_4{\cdot}6H_2O$. Li et al. [59] utilized a novel burning raw material (BRM) as an intermediate product for stabilizing PO_4^{3-}-P and F^- in phosphogypsum. Under a phosphogypsum-to-BRM ratio of 100:2 and a solid-to-liquid ratio of 4:1, the phosphogypsum leachate exhibited an F^- concentration of 8.65 mg/L and a PO_4^{3-}-P stabilization efficiency of 99.78% after a 24-h reaction at 30 °C. The stabilized compounds primarily included $Ca_5(PO_4)_3F$, $CaPO_3(OH)$, $Ca_5(PO_4)_3(OH)$, $Ca_2P_2O_7{\cdot}2H_2O$, $CaSO_4PO_3(OH){\cdot}4H_2O$, CaF_2, and $CaFPO_3{\cdot}2H_2O$.

2.3.3. Recovery of Valuable Elements

The recovery of valuable elements from IISWs requires a secondary extraction of resources, which can increase their value. The recovery of Fe and Al from solid waste is common. Li et al. [60] recovered Fe and Al from red mud using acid leaching, with recoveries exceeding 90% and 92%, respectively. Some heavy metals are present in solid waste. Zhang et al. [61] leached copper smelting dust (CSD) with sulfuric acid, achieving leaching ratios of 87.23%, 93.07%, and 95.21% for Cu, Zn, and As, respectively. This method successfully recovered valuable metals from CSD. Rare metals in IISWs are also an important part of recycling. Habibi et al. [62] employed a process involving washing, calcination, hydrolysis, and solvent extraction to recover REEs and Ti from red mud. The total Sc recovery reached 83.8%, and the total Ti recovery was 78.5%. Zeng et al. [35] investigated REE leaching in phosphogypsum, achieving a recovery of 83.4% for ∑REE at 80 °C.

2.3.4. Producing Various Materials

To meet the growing trend of waste reuse and clean production, many studies have used IISWs containing substances such as quartz, gypsum, alumina, and calcium oxide to prepare cementitious materials, geopolymers, permeable bricks, and subgrade materials.

Using solid waste rather than traditional raw materials to produce cementitious materials can reduce carbon emissions and resource consumption, which is of great significance to the development of green building materials. Li et al. [63] synthesized cement-based materials using red mud and arsenic sludge. Under optimal conditions, the compressive strength of the cement-based material reached 12.05 MPa after 28 days of curing. He et al. [64] prepared ternary composite cementitious materials using activated electrolytic manganese residue (AEMR), slag, and cement. For these ternary mortars, the compressive strength was significantly higher than that of the AEMR-cement binary system. Additionally, the microstructure of the ternary system mortar was superior to that of the AEMR-cement binary system mortar. Luo et al. [24] developed a novel iron phosphate cement (IPC) using CSS and ammonium dihydrogen phosphate (ADP) as starting materials. The prepared IPC material holds significant potential as an alternative cementitious material for pavement and building restoration applications. Ouyang et al. [65] prepared a phosphogypsum-based all-solid-waste cementitious binder using steel slag powder as an alkaline activator. Lian et al. [66] utilized phosphogypsum as the primary raw material for a high-content phosphogypsum cementitious (HCPC) system. In this system, phosphogypsum serves as the 'skeletal support,' providing the fundamental components for hydration reactions. Ke et al. [67] utilized the synergistic effects of low-quality IISWs such as circulating fluidized bed fly ash (CFBFA), red mud, fly ash (FA), and carbide slag (CS) to produce long-term, performance-stable, eco-cementitious materials. The materials exhibit excellent early strength, no cracking, and favorable, stable strength development in later stages. Wang et al. [68] prepared red mud-phosphogypsum-based composite cementitious materials (RM-PGCM) using red mud and hemihydrate phosphogypsum as cement substitutes. The composite with 7% red mud and 60% hemihydrate phosphogypsum exhibited optimal performance, achieving a 28-day compressive strength of 23.33 MPa, flexural strength of 7.68 MPa, softening coefficient of 0.75, and thermal conductivity of 0.3765 $W \cdot m^{-1} \cdot K^{-1}$.

The development of solid waste-based polymers effectively addresses the challenge of waste accumulation, with its superior performance offering a novel solution for engineering applications. Luo et al. [69] prepared single-component polymers using lithium slag as the raw material, combined with composite activators NaOH–Na_2SiO_3, NaOH–$Ca(OH)_2$, and NaOH–$CaCO_3$. Experimental results demonstrated that the lithium slag-based polymer with 5% composite activator could achieve moderate mechanical properties, as evidenced

by a compressive strength of up to 35.6 MPa at 28 days. Li et al. [70] synthesized geopolymer by using EMR and lead-zinc smelting slag (LZSS) as raw aluminum silicate materials. The results showed that the geopolymer loaded with 1% $Pb(NO_3)_2$ exhibited the highest 7-day compressive strength of 28.5 MPa, with heavy metal leaching concentrations below the limits (total Pb < 5 mg/L; total Zn < 100 mg/L). Xu et al. [71] utilized red mud to produce engineered geopolymer composites (EGC) with high strength and high ductility. The research results demonstrated that EGC containing 50% high red mud achieved a compressive strength exceeding 100 MPa and a tensile strain capacity of over 5%. Li et al. [72] developed a novel ternary, fly ash-based geopolymer by recycling red mud and BFS. This geopolymer exhibits considerable mechanical strength and significant environmental advantages.

Solid waste is the main raw material for preparing sintered or non-fired brick, which can reduce the exploitation of natural resources, relieve pressure on solid waste accumulation, and provide both economic and environmental benefits. Zhao et al. [73] incorporated red mud into calcium sulfoaluminate cement to produce unsintered bricks. The red mud effectively reduced the porosity of the hydration products in the binary mixture, thereby enhancing the bricks' compressive strength in the later hydration age. Zhou et al. [74] utilized phosphogypsum as the sole raw material to fabricate hardened bricks through an innovative batch pressing hydration process. Under optimal pressing conditions, the resulting hardened tiles achieved a high flexural strength of 18.9 MPa. Pahroraji et al. [75] prepared brick samples using coal ash, including CFA and bottom ash, as the raw materials, and ground granulated blast-furnace slag (GGBS) and hydrated lime as binders. The silica-rich CFA contributes to hardness, while the calcium oxide and silica-rich slag not only enhances hardness but also acts as a catalyst to promote strength formation.

The development and application of solid waste-based subgrade materials represent an organic integration of transportation infrastructure and solid waste resource utilization, offering innovative solutions for low-carbon infrastructure. Wang et al. [76] developed an EMR-based subgrade material using EMR, carbide slag, and GGBS as raw materials. The optimal pretreatment ratio of carbide slag to EMR was 1:9. The carbide slag-pretreated EMR stabilized with 10% GGBS exhibited high strength and excellent durability, achieving a strength exceeding 10 MPa after 7 days of curing. Wang et al. [77] developed a composite cement-based system combining phosphogypsum with a small amount of inorganic curing agents, particularly emphasizing waterproofing components, along with cement and GGBS, to enhance road performance and water stability. Under the optimal proportion, the compaction characteristics and water stability of the subgrade materials met the highway engineering standards.

3. Preparation of Adsorbents from IISWs

IISWs containing elements such as Si, Al and Fe can serve as potential raw materials for adsorbent production. Typically, processes such as alkali melting and hydrothermal treatment are employed to convert these IISWs into adsorbents [78]. The produced adsorbents mainly include modified IISWs, zeolites, silica particles, metal oxides, porous ceramics, and composite and hybrid adsorbents.

3.1. Modified IISWs

IISWs may generate adsorption active sites during their production process, endowing them with inherent adsorption properties. Zhong et al. [6] tested the adsorption performance of red mud, with a maximum adsorption capacity (q_m) of 0.28 mmol·g^{-1}. Han et al. [30] used spodumene leaching residue (SLR), a kind of lithium slag, as an adsorbent. SLR possesses a structure with active adsorption sites, exhibiting a specific memory effect for lithium ions. Based on the compositions of β-lithium pyroxene and SLR, a crystal structure model

was established using Materials Studio 6.0, as shown in Figure 1A. However, the direct application of untreated IISWs in adsorption applications may lead to contamination and often results in limited efficacy. Therefore, such wastes must undergo modification before use in adsorption. Surface chemical modification with reagents, hydrothermal treatment, and pyrolysis are common methods for altering the composition and phase composition of IISWs, thereby enabling resource utilization and enhancing their adsorption performance.

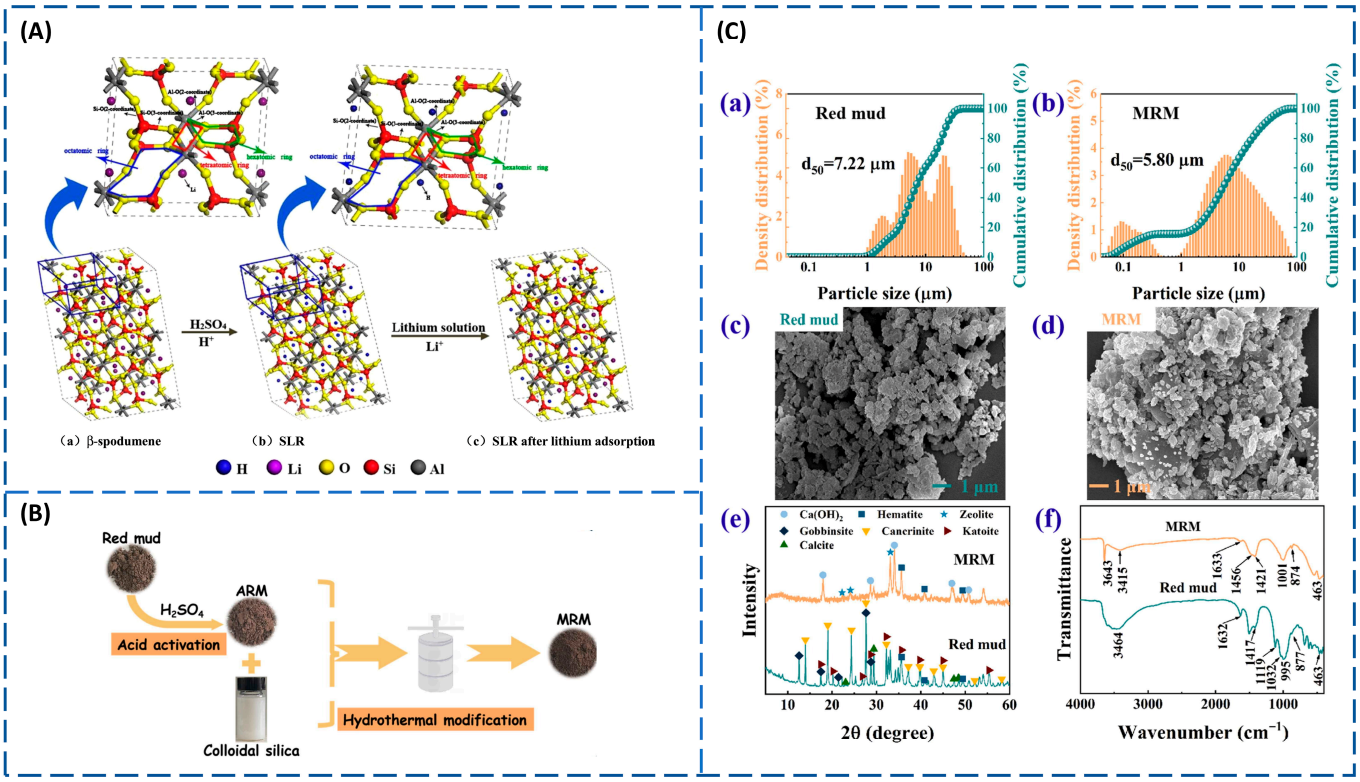


Figure 1. (**A**) Crystal structure diagrams of (a) *β*-spodumene (b) spodumene leaching residue (SLR), and (c) SLR after Li adsorption. Reprinted with permission from reference [30]. Copyright 2018, Elsevier. (**B**) Preparation procedure of activated red mud (ARM) and modified red mud (MRM). (**C**) Characterization of red mud and MRM: (**a**,**b**) Particle size distributions, (**c**,**d**) Scanning electron microscopy (SEM) images, (**e**) X-ray diffraction (XRD) patterns, and (**f**) Fourier transform infrared spectroscopy (FTIR) spectra. Reprinted with permission from reference [6]. Copyright 2024, Elsevier.

Surface chemical modification typically involves activating or etching IISWs with acids, alkalis, salts, or organic compounds, thereby exposing more atoms and generating additional active sites. Zhong et al. [6] treated red mud with sulfuric acid and obtained an activated red mud (ARM) adsorbent with a maximum adsorption capacity of 0.46 mmol·g^{-1} for Ni^{2+}, which was higher than that of the original red mud. Zhang et al. [79] prepared a high-performance CaO/$C_{12}A_7$ high-temperature calcium-based CO_2 adsorbent by activating ladle furnace (LF) refining slag with acetic acid leaching and high-temperature calcination. The adsorbent primarily consists of CaO, with a dispersed amount of $C_{12}A_7$. As the inert framework of the adsorbent material, $C_{12}A_7$ inhibits CaO particle agglomeration and slows the sintering deactivation process. $C_{12}A_7$ increases the number of oxygen vacancies in the CaO lattice of the CaO/$C_{12}A_7$ calcium-derived adsorbent, thereby enhancing CO_2 diffusion and O_2 migration during the early stages of diffusion-controlled carbonation, ultimately improving the carbon dioxide capture capacity of CaO. Shi et al. [80] prepared a sodium hydroxide-activated coal gasification coarse slag (SH-CGCS) from coal gasification coarse slag (CGCS) via alkali activation. SH-CGCS is a mesoporous material with a mesoporous content over six times that of CGCS and a specific surface area (64 m^2·g^{-1}) ap-

proximately six times that of CGCS (11 $m^2 \cdot g^{-1}$). Compared to CGCS, its adsorption capacity is significantly enhanced. Wei et al. [81] employed a mechanical dispersion-suspension solidification method, using Fe-rich CSS as a raw material and a sodium silicate-sodium hydroxide mixture as an alkali activator. By regulating the mechanical stirring speed to control the particle size of the adsorbent, they successfully prepared a magnetic copper slag-based alkali-activated microspheres (CS-AAMs). Ning et al. [82] prepared an iron-modified water treatment residue (Fe-WTR) by mixing $FeCl_3$ solution with water treatment residue (WTR), followed by drying, washing, and grinding. Compared with WTR, Fe-WTR exhibits a rougher surface and more dispersed particle distribution, with its surface area increasing from 34.19 $m^2 \cdot g^{-1}$ to 50.29 $m^2 \cdot g^{-1}$. This heterogeneous morphology provides Fe-WTR with more surface active sites for adsorption. Ifthikar et al. [83] modified wastewater treatment sewage sludge biochar with carboxymethyl chitosan to develop a CMC-SSBC-3 biosorbent. Carboxymethyl chitosan coating on sewage sludge biochar improved its stability in water, enabling the biosorbent to demonstrate excellent reusability for heavy metal ions, including Pb^{2+} and Hg^{2+}.

Hydrothermal treatment of IISWs facilitates their phase transformation, thereby enhancing their adsorption performance. Zhong et al. [6] used a hydrothermal method to treat ARM with sodium hydroxide and colloidal silica, obtaining a modified red mud (MRM). The preparation and characterization of MRM are shown in Figure 1B,C. The maximum adsorption capacity of MRM for Ni^{2+} was significantly higher than that of the original red mud and ARM.

Pyrolysis can decompose certain components in IISWs at high temperatures, thereby generating more porous channels and increasing their specific surface area. Zhou et al. [28] prepared a novel red mud-based adsorbent by calcining red mud in a nitrogen-filled tubular furnace, which is used to remove low-concentration carbonyl sulfide (COS) from flue gas. The active components include active alkali, FeOOH, and Fe_3O_4. Cao et al. [47] employed a template synthesis method using red mud and polystyrene (PS) microspheres as raw materials. By calcining in air to remove the PS template, they successfully synthesized modified red mud with PS (MRM-PS) featuring a hierarchical macroporous–mesoporous structure. The resulting nanoparticle system exhibits high surface area and uniform pore size distribution, with red mud and MRM-PS demonstrating surface areas of 8 $m^2 \cdot g^{-1}$ and 232 $m^2 \cdot g^{-1}$, respectively, and total pore volumes of 0.02 $cm^3 \cdot g^{-1}$ and 0.27 $cm^3 \cdot g^{-1}$, respectively. The modification process decomposes hydrogarnet and cancrinite in red mud, removing most of the calcium and sodium. Qiu et al. [84] mixed CFA with biomass and subjected it to pyrolysis, followed by pH adjustment using sodium hydroxide and hydrochloric acid solutions. The treated sample exhibited an increased surface area and more adsorption sites, demonstrating strong adsorption capacity for Cu^{2+} in aqueous solutions.

3.2. Porous Aluminosilicates and Silicon/Metal Oxides

Most IISWs are rich in Si and Al elements. Therefore, aluminosilicates and oxides, such as zeolites, micro- and nano-silica, and metal oxides, can be obtained from IISWs. These materials feature T–O (T = Si and/or Al) bond structures that form micro/nano pores and exhibit micro/nano-sized architectures with high specific surface areas, endowing them with inherent advantages as adsorbents.

3.2.1. Zeolites

Zeolites are three-dimensional crystalline materials formed by tetrahedral SiO_4 and AlO_4 units linked through shared oxygen atoms in a specific sequence [5]. Their large specific surface area and molecular-scale pores make zeolites widely used in adsorption and catalysis. In adsorption applications, zeolites can capture waterborne dyes [85], metal

ions [86], phenols [87], and other substances. IISWs rich in Si and Al are ideal raw materials for low-cost zeolite production. The application of solid waste-derived zeolites in pollution control achieves dual environmental protection, offering a win–win solution. The two-step method is the preferred procedure for converting IISWs into zeolites. In this process, IISWs are first subjected to alkali melting pretreatment, followed by hydrothermal treatment. During the conversion, the insoluble glass phase and the crystalline phase are eliminated, and the aluminosilicate zeolite framework forms.

The most common method for converting IISWs into zeolites is the hydrothermal method. Ibsaine et al. [88] developed a NaX zeolite with excellent ion exchange capacity via the hydrothermal method using lithium slag. The research identified fine particles as the optimal component for zeolite production, with over 56% of the lithium slag containing particles smaller than 53 μm. Compared to the initial lithium slag, the synthesized zeolite showed a reduced Si/Al ratio from 2.06 to 1.22–1.47, while Na_2O content increased significantly from 0.13% to 17.8–23.1%. Lv et al. [89] used lithium slag as a raw material to synthesize zeolite NaA via a conventional hydrothermal method, and they applied the resulting zeolite to the adsorption of Pb^{2+} and Cd^{2+} from heavy metal wastewater. Li et al. [33] used EMR and red mud as raw materials, adjusting the system's alkalinity by using sodium hydroxide solution during the crystallization process, with the final product being zeolite X (ERZ). The results demonstrated that the synthesized ERZ exhibited excellent crystallinity, high thermal stability, and a large specific surface area. Figure 2A showed that ERZ exhibited a typical octahedral structure with regular morphology. Figure 2B indicated that at 0–1 h of crystallization, the peaks of the Raman spectra at 502 cm^{-1} and 576 cm^{-1} corresponded to four-membered rings (4Rs) and branched 4Rs, respectively, while the peak at 848 cm^{-1} was the symmetric stretching vibration peak of the T–O bond, and the peak at 1007 cm^{-1} was the asymmetric stretching vibration peak of the T–O–T bond (indicating the presence of β cages). After 3 h, the 4Rs peak sharpened and shifted to 511 cm^{-1}, with the appearance of double six-membered ring (D6R) bending vibration peaks at 284 cm^{-1} and 380 cm^{-1}. After 6 h, the characteristic peaks of zeolite X appeared at 289 cm^{-1}, 378 cm^{-1}, 985 cm^{-1}, and 1076 cm^{-1}, with 985 cm^{-1} and 1076 cm^{-1} corresponding to the asymmetric stretching vibration of the T–O–T bond. Figure 2C demonstrates that the N_2 adsorption–desorption isotherm of ERZ exhibits an I-type isotherm with a H4-type hysteresis loop, indicating its microporous structure dominated by monolayer adsorption. The specific surface area reaches 512.679 $m^2 \cdot g^{-1}$, with a pore volume of 0.297 $cm^3 \cdot g^{-1}$ and a micropore diameter of approximately 1.874 nm. The large specific surface area and suitable pore size endow it with excellent potential for ion exchange and pollutant adsorption. Figure 2D shows that before crystallization, the sample exists as an amorphous silico species, with a broad peak at −83.2 ppm in chemical shift, decomposing into four sub-peaks, Si(4Al) (sodalite), Si(4Al), Si(3Al), and Si(2Al), indicating the presence of β-lattice and 4Rs structural units. After 3 h, the primary coordination structures of Si are Si(4Al), Si(3Al), and Si(2Al), suggesting that the silico species undergoes depolymerization to form cyclic or chain-like structures. After 6 h, distinct peaks appear at −84.0 ppm and −89.2 ppm, with the primary coordination structures being Si(4Al) and Si(3Al). The peak shapes become sharper with increasing crystallization time, reflecting enhanced crystallinity. Before crystallization, a broad peak appeared at 61.8 ppm, corresponding to the Al(4Si) and Al(3Si) species in the amorphous silicoaluminate phase. As the crystallization time increased, the proportion of Al(4Si) increased, the peak shape gradually narrowed, and the structural order improved, ultimately forming a tetrahedral Al structure within the zeolite X framework. Ma et al. [43] initially synthesized a geopolymer using CFA and ladle furnace slag (LFS), followed by hydrothermal treatment, to produce zeolite. The zeolite primarily consists of kieselsite, sodium feldspar, zeolite-P, and trace amounts of hydrated

calcium silicate gel, which effectively removes Pb^{2+} from wastewater. Sun et al. [90] utilized a CGS-derived desilication solution as the primary silicon and sodium source to synthesize ZSM-5 zeolite via a one-step hydrothermal method. The optimized ZSM-5 zeolite exhibited hexagonal morphology with a well-defined crystalline structure, demonstrating a relative crystallinity of 101.48%, a specific surface area of 337.48 $m^2 \cdot g^{-1}$, and a pore volume of 0.190 $cm^3 \cdot g^{-1}$. Characterized by an exceptional silicon-to-aluminum ratio, the zeolite achieved a SiO_2/Al_2O_3 molar ratio of 104.93.

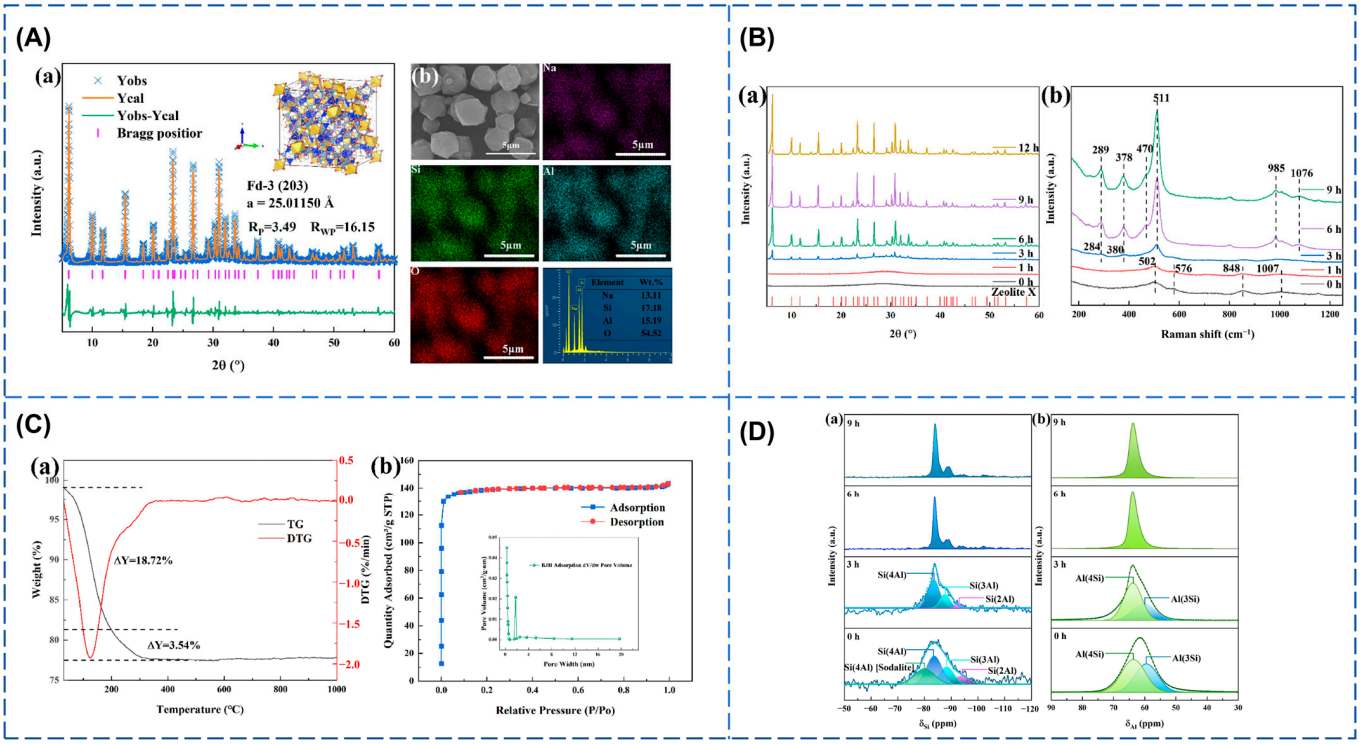


Figure 2. Characterization of zeolite X: (**A**) (**a**) Rietveld refinement and (**b**) SEM mapping of elemental distribution and energy-dispersive X-ray spectroscopy (EDS) spectrum; (**B**) (**a**) XRD patterns and (**b**) Raman spectra of samples at different crystallization time; (**C**) (**a**) Thermogravimetric analysis (TG) curve and (**b**) N_2 adsorption–desorption isotherm; (**D**) (**a**) ^{29}Si and (**b**) ^{27}Al solid-state nuclear magnetic resonance (SSNMR) spectra of samples at different crystallization time. Reprinted with permission from reference [33]. Copyright 2025, Elsevier.

Before the hydrothermal synthesis of zeolites, pretreatment of IISWs, such as through alkali dissolution, is sometimes required. Li et al. [12] used silicon and aluminum extracted from red mud as raw materials, adding $Na_2SiO_3 \cdot 9H_2O$ or $NaAlO_2$ to adjust the Si/Al molar ratio to 1.05. The adjusted mixture was transferred to a high-pressure reactor lined with polytetrafluoroethylene (PTFE) and subjected to hydrothermal treatment at 95 °C for 12 h. After the hydrothermal reaction, the white solid product was collected by filtration, thoroughly washed with deionized water and ethanol, and dried to obtain an RML-NaA zeolite. The RML-NaA zeolite material appeared as a white powder, exhibiting excellent crystallinity and the typical cubic structure of NaA zeolite, with a specific surface area of 18.02 $m^2 \cdot g^{-1}$. Chen et al. [91] synthesized NaP1 zeolite from red mud through alkali fusion followed by hydrothermal treatment, and the resulting zeolite exhibited excellent adsorption performance for methylene blue (MB). Chen et al. [92] synthesized zeolite X with a crystallinity of 94.31% from lithium slag via an alkaline melt hydrothermal reaction. This octahedral crystal exhibits excellent thermal stability, with a specific surface area of 847 $m^2 \cdot g^{-1}$ and a main pore size of 0.859 nm. Wang et al. [93] investigated the conversion of lithium slag into high-crystallinity hydroxysodalite, NaX zeolite, and NaA zeolite without

the use of template agents or seed crystals. The process consists of two steps: an alkaline melting reaction and a crystallization reaction. The alkaline melting reaction involves mixing NaOH with lithium slag and heating the mixture in a muffle furnace at high temperature. The crystallization reaction combines the resulting light-blue crystals with deionized water and subjects them to autoclaving to achieve zeolite crystal growth and stabilization. Ultimately, the conversion rates of the primary elements aluminum and silicon in these zeolites both exceeded 90%. Li et al. [16] synthesized a porous zeolite (EMRZ) using silicon-rich flotation concentrate (EMRC) as a raw material. Through silicon extraction and subsequent hydrothermal treatment, pure, single-phase, spherical zeolite P was successfully synthesized. Under optimal conditions, the obtained zeolite P exhibited an average specific surface area of 52.46 $m^2 \cdot g^{-1}$ and a total pore volume of 0.042 $cm^3 \cdot g^{-1}$. Li et al. [32] used EMR as raw material to synthesize highly crystalline zeolite A (EMRZA) and zeolite X (EMRZX). The synthesis employed a two-step process involving alkaline fusion and hydrothermal methods. Li et al. [94] synthesized zeolites using EMR as the source of Si and Al via an alkaline fusion-hydrothermal method. The product with a Si/Al ratio of 1.5 was composed of NaA zeolite with a specific surface area of 35.38 $m^2 \cdot g^{-1}$. With the increase in the Si/Al ratio from 1.5 to 2.5, the crystallinity and phase purity of the samples decreased. Li et al. [39] prepared a BFS-derived zeolite (BFSZ) from BFS using an alkali fusion–hydrothermal synthesis method. The product contains NaA zeolite with a well-developed surface and a particle size of approximately 2 μm, primarily composed of Si, Al, O, and Na. Under a crystallization time of 4–8 h, the zeolite content in BFSZ reached 90.90–97.41%. Acid treatment is an essential step for preparing zeolite precursors with ideal compositions from steel slag. Kuwahara et al. [95] used steel slag as a raw material and achieved a well-crystallized Na-type FAU zeolite, a type of zeolite including zeolite X and zeolite Y, by removing CaO through acid treatment, followed by hydrothermal treatment. Feng et al. [22] converted CFA into high-crystalline zeolite A with a typical cubic microstructure via a two-stage fusion and hydrothermal treatment. The toxic heavy metals in the synthesized zeolite were partially immobilized, with leaching concentrations below the WHO safe drinking water limits. This CFA-derived zeolite exhibited high removal efficiency for cesium and strontium in simulated polluted water. Liu et al. [42] utilized CFA as a raw material and employed a high-speed dispersion homogenization-assisted alkali fusion–hydrothermal method to synthesize NaA zeolites with excellent ammonia nitrogen adsorption performance. The zeolites prepared under calcination at 700 °C and crystallization at 80 °C exhibited good crystallinity and high purity, characterized by a uniform, orderly, and well-defined cubic prismatic crystal structure, with a specific surface area as high as 288.219 $m^2 \cdot g^{-1}$. Ameh et al. [96] prepared NaA zeolites with different crystal sizes and crystallinity by using a two-step method of alkali melting and hydrothermal synthesis using CFA as a raw material. The crystal size of NaA zeolites (0.67–3.18 μm) could be controlled by adjusting the Si/Al ratio (0.27–0.80) in the synthesis mixture. The primary crystalline phases in the original CFA included mullite, quartz, hematite, and magnetite. Notably, when compared with molten CFA, the mullite, quartz, and hematite mineral phases in the original CFA were completely converted into two new mineral phases: aluminates (Na_2AlO_2) and silicates (Na_2SiO_3). The synthesis of zeolites from inorganic solid waste serves as a crucial pathway to achieve synergistic resource utilization and high-value material production. Alkaline melting pretreatment is widely adopted due to its ability to efficiently activate silicoaluminous components and enhance zeolite crystallinity. However, this process typically requires high-temperature calcination and strong alkaline media, accompanied by significant energy consumption and alkali solution usage. The resulting environmental burden and energy costs have become key constraints for green and large-scale application of the process. Current research predominantly

focuses on activation efficiency and product performance, while lacking systematic analysis and quantitative evaluation of energy consumption, carbon emissions, and environmental impacts during the pretreatment stage.

During hydrothermal synthesis, microwave irradiation can enhance the process. Huang et al. [15] directly used lithium slag with a SiO_2/Al_2O_3 molar ratio of 4.22, low impurity content (iron, calcium, etc.), and a single crystal structure as a raw material for synthesizing NaX zeolites without pretreatment or silicon–alumina source supplementation. NaX zeolites were synthesized via hydrothermal and microwave-assisted methods. Results demonstrated that the microwave-assisted synthesis method offered significant advantages, reducing synthesis time to only 36% of that for hydrothermal synthesis while maintaining the same synthesis mechanism and product properties. The synthesis process and proposed mechanisms are illustrated in Figure 3. At the initial stage, the β-lithium pyroxene structure after Li^+ leaching was disrupted by NaOH, causing lithium slag dissolution to form Si–O tetrahedrons and Al–O tetrahedrons. Simultaneously, these reacted to form sodium silicoaluminate, with Al(VI) transitioning to Al(IV) and silicon species initiating Al coordination. At the intermediate stage, under OH^- influence, Si–O tetrahedrons and Al–O tetrahedrons condensed to form silicoaluminate gel, which further assembled into D6R secondary structures. D6R aggregation formed nuclei that grew into NaX crystals, with simultaneous lithium slag dissolution, gel formation, and crystal growth. At the late stage, the complete dissolution of lithium slag transformed all silicoaluminate gels into D6R structures, ultimately forming pure-phase NaX zeolite crystals. Microwave accelerated the polarization of polar species (Si and Al species) by converting electromagnetic energy to thermal energy, enhancing heat and mass transfer efficiency while shortening reaction times across stages without altering species transformation pathways. Fukasawa et al. [97] investigated the effects of pulverization and aluminum addition on the microwave-hydrothermal synthesis of CFA-derived zeolites at 373 K. The results indicated that pre-pulverization of CFA before heating increased the yield of by-products. When heating and pulverization were conducted simultaneously, the zeolite formation rate was higher within the first hour of pulverization but decreased with prolonged pulverization. A lower aluminum ion content hindered the formation of the zeolite precursor, the alumino-silicate gel. Therefore, adding aluminum ions to the slurry enhanced the zeolite formation rate. However, excessive aluminum ions led to increased by-product formation, which adversely affected the subsequent adsorption of ammonium ions.

3.2.2. Silica Particles

The integration of resource utilization of IISWs with micro/nanomaterial preparation holds significant importance. Utilizing IISWs as raw materials to produce micro/nanosilica particles not only mitigates pollution from waste storage but also reduces material costs, offering both environmental and economic benefits with broad application prospects. Bang et al. [98] employed acid leaching to remove alkali metal ions from BFS, ultimately yielding a high-purity (~99%) amorphous silica powder with a wide specific surface area. Gao et al. [99] synthesized mesoporous silica materials with specific surface areas of 475.93 $m^2 \cdot g^{-1}$ and 642.57 $m^2 \cdot g^{-1}$ from activated CFA with potassium silicate and $KAlSiO_4$–O1 phase crystalline structures. This synthesis procedure was carried out by using a template-free method involving a two-step mineral phase transformation and selective acid etching. Jankowska et al. [100] synthesized ordered mesoporous silica materials, MCM-41 and SBA-15, via a template method, using CFA as the silicon source and cetyltrimethylammonium bromide (CTAB) as a template agent. The pure MCM-41 exhibited a specific surface area of 991 $m^2 \cdot g^{-1}$, and a total pore volume of 0.84 $cm^3 \cdot g^{-1}$. The pure SBA-15 had a specific surface area of 802 $m^2 \cdot g^{-1}$, and a total pore volume of 0.88 $cm^3 \cdot g^{-1}$.

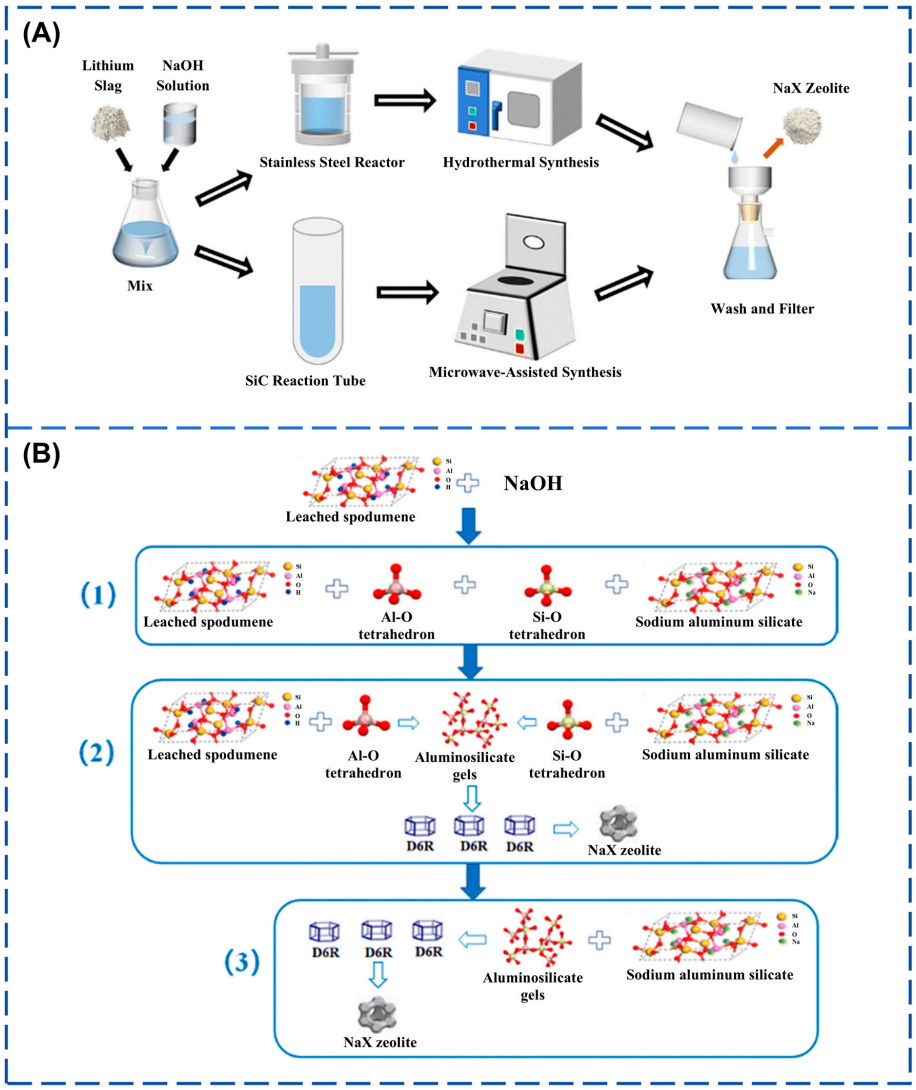


Figure 3. (**A**) The process of synthesizing zeolite from lithium slag. (**B**) The possible mechanisms for synthesizing zeolite from lithium slag. Reprinted with permission from reference [15]. Copyright 2023, The Royal Society of Chemistry.

3.2.3. Metal Oxides

Most IISWs are rich in Al, Fe, Ti and other elements and serve as economical raw materials for the preparation of metal oxide adsorbents. Numerous studies on the preparation of metal oxide adsorbents from IISWs have been conducted and published. Liu et al. [101] first leached red mud with sulfuric acid to open closed pores and release metal ions such as Fe^{3+} and Al^{3+}. They then added a complex base saturated solution to the leaching solution to precipitate Fe^{3+} and Al^{3+} completely. The resulting Fe-Al adsorbent was rich in mesoporous structures. The composition of the Fe-Al adsorbent is centered around the amorphous Fe-Al (hydroxide) formed in situ. This adsorbent exhibited a BET specific surface area of 63.59 $m^2 \cdot g^{-1}$, a total adsorption pore volume of 0.0987 $cm^3 \cdot g^{-1}$, and an average pore diameter of 4.2390 nm. Shon et al. [102] calcined the sludge produced by aluminum sulfate ($Al_2(SO_4)_3$), ferric chloride ($FeCl_3$), and titanium tetrachloride ($TiCl_4$) flocculation at 1000 °C, 700 °C, and 600 °C, respectively. The corresponding phases of the calcined products are mainly alumina, hematite and grattarolaite ($Fe_3(PO_4)O_3$ or Fe_3PO_7), and titanium oxide (TiO_2), respectively. Chen et al. [103] developed an innovative three-step method to synthesize NiO@γ-Al_2O_3 composite materials from WTS. The raw material, primarily composed of SiO_2, contains various forms of aluminum. Through high-temperature

calcination, unstable metal components are transformed into stable metal oxides, and organic compounds are decomposed. Subsequently, NiO nanocrystals grow in situ on the calcined sludge, followed by calcination to form a porous structure. The resulting NiO@γ-Al_2O_3 composite exhibits hierarchical porosity and self-assembled NiO nanosheets. Compared to initial sludge particles, the composite's specific surface area increased by 5–6 times, providing more adsorption sites. This composite demonstrates high efficiency in cadmium removal.

3.3. Porous Ceramics

Porous ceramics have significant potential for adsorption applications due to their high porosity, extensive surface area, excellent thermal and wear resistance, superior mechanical properties, and strong regenerability [104]. Studies confirm that these ceramics can efficiently remove metal ions from wastewater through multiple mechanisms, including surface complexation, ion exchange, and physical adsorption. IISWs contain a large amount of Al/Si-derived components, making them suitable, low-cost raw materials for the preparation of porous ceramics. Currently, many resource recovery methods for IISWs involve preparing ceramics from solid waste. The standard procedure for producing porous ceramics via a pore-forming agent method involves mixing matrix materials with binders and pore-forming agents, followed by high-temperature sintering to obtain the final product. Depending on the type of pore-forming agent, this method can be categorized into organic and inorganic approaches, with some preparation processes requiring no additional pore-forming agents.

Inorganic pore-forming agents are chemically stable and do not easily agglomerate during mixing. Some of these agents decompose to produce gases, which can form double pores. Deng et al. [105] prepared red mud-derived ceramics by mixing red mud, bentonite binder, and $CaCO_3$ in specific proportions, followed by high-temperature calcination in a muffle furnace. The resulting ceramics exhibited a pore-size distribution ranging from 0 to 200 nm, with the majority of pores (0–50 nm) being mesoporous. During calcination, certain metal minerals in the red mud underwent phase transformations, with Fe primarily existing as hematite. Concurrently, new minerals such as aluminum iron oxide ($Al_3Fe_5O_{12}$) and nepheline ($Na[AlSiO_4]$) were formed. Wu et al. [106] converted EMR into a porous ceramic adsorbent for methylene blue adsorption through four steps: raw material pretreatment, mixing, forming, and sintering. The pore-forming agent, carbon powder, decomposes or burns during sintering, producing gases that escape and form numerous pores within the ceramic, endowing it with a porous structure. The finished ceramic exhibited a compressive strength of 6.97 MPa, an apparent porosity of 69.70%, a specific surface area of 0.897 $m^2 \cdot g^{-1}$, and predominantly mesoporous pores (an average pore size of 3.433 nm), enabling efficient adsorption of methylene blue molecules. Ma et al. [107] successfully prepared porous mullite ceramics using a reactive synthesis process with CFA as the primary raw material. During sintering, SiC reacts with O_2 to produce products such as SiO_2, CO_2, SiO, and CO. The escape of gaseous products forms pores, while the generated SiO_2 participates in mullite synthesis, thereby regulating the pore structure.

Organic pore-forming agents are readily decomposable and removable, and can regulate pore size and porosity. They are widely available and cost-effective, enabling the creation of ideal pore structures in materials. Li et al. [108] fabricated ceramic membranes using red mud and bentonite as raw materials, with polymethyl methacrylate (PMMA) as a pore-forming agent, through a dry pressing–solid-state sintering process. The abundant oxides in red mud, including SiO_2, Al_2O_3, Fe_2O_3, and Na_2O, undergo complex solid-phase reactions during high-temperature sintering, forming crystalline phases such as hematite, nepheline, and sodium-potassium-aluminum silicate, which constitute the framework

structure of the ceramic membrane. As a sacrificial pore-forming agent, PMMA decomposes and is completely removed at approximately 400 °C, with the space it occupies forming interconnected pores.

Some preparation processes do not add extra chemical pore-forming agents but achieve a porous structure through physical and chemical changes in the raw materials themselves and during calcination. Huang et al. [109] developed red mud-based modified ceramsites (RMMC) using red mud and desulfurization gypsum whiskers (DGW) as raw materials through hydrothermal synthesis pretreatment and high-temperature calcination. The preparation process and characterization of RMMC are shown in Figure 4. During calcination, the crystallization water in DGW is largely removed and volatilized, creating abundant pores within the ceramic. The silane coupling agent KH550 fully decomposes during calcination, releasing trace gases that further promote pore formation. The Fe_2O_3, SiO_2, and Al_2O_3 in red mud react with CaO produced by DGW decomposition to form aluminosilicate minerals and glassy phases, establishing a robust framework structure. This framework prevents pore collapse and ensures the stability of the porous architecture. Cusido et al. [110] prepared ceramic particles by drying wastewater treatment plant sludge and subsequently subjecting it to ceramicization at 1050 °C. The sludge particles contained 65% residual organic matter and 5% residual moisture. During sintering, the organic matter decomposed and burned, releasing steam and volatile gases that escaped from the particle interior to the surface. Simultaneously, the expansion force generated by the combustion of organic matter maintained the spherical morphology of the particles, ultimately leaving numerous pores in the ceramic matrix, thereby forming a porous structure.

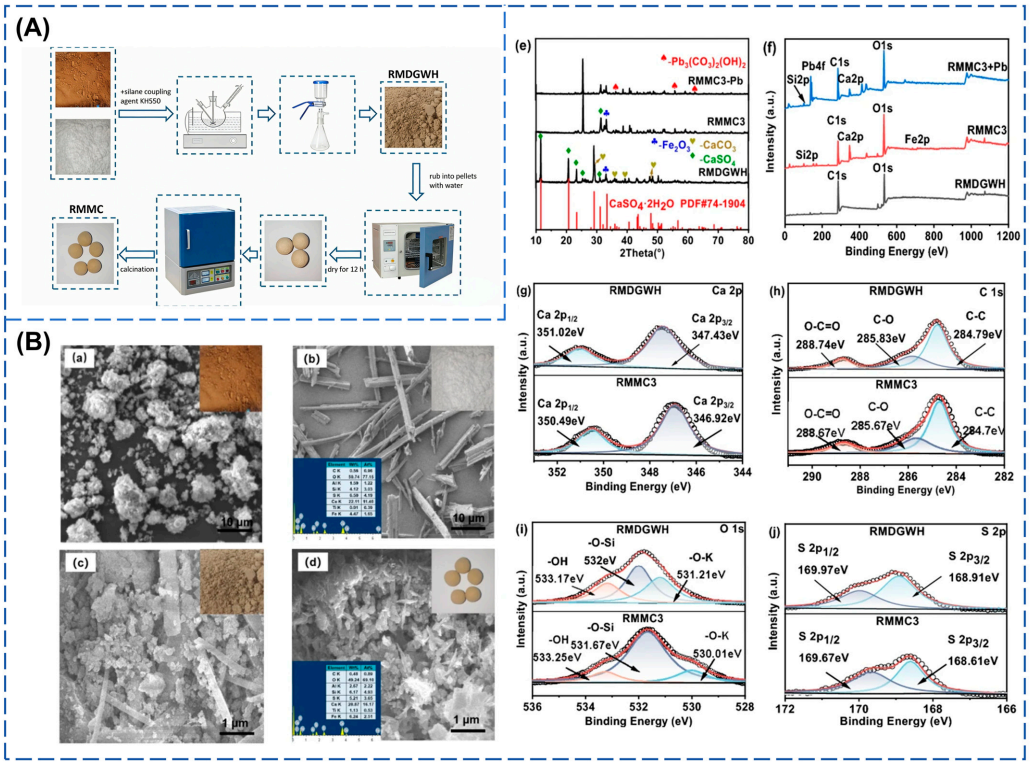


Figure 4. (**A**) Preparation process of red mud-based modified ceramsites (RMMC). (**B**) Characterization of RMMC: SEM images of (**a**) red mud, (**b**) desulfurization gypsum whiskers (DGW), (**c**) intermediate of RMMC (RMDGWH), and (**d**) RMMC3; (**e**) XRD of $CaSO_4 \cdot 2H_2O$, RMDGWH, RMMC3, and RMMC3-Pb; (**f**) X-ray photoelectron spectroscopy (XPS) spectra of RMDGWH, RMMC3, and RMMC3-Pb; High-resolution XPS spectra of RMMC3 and RMDGWH for (**g**) Ca 2p, (**h**) C 1s, (**i**) O 1s, and (**j**) S 2p. Reprinted with permission from reference [109]. Copyright 2025, Springer Nature.

3.4. Composite and Hybrid Adsorbents

To improve the utilization of IISWs, researchers often mix different types of IISWs to prepare composite adsorbents. These composite adsorbents typically exhibit multifunctional adsorption properties.

3.4.1. Inorganic Solid Waste Composites

The synergistic combination of multiple IISWs enables the design of composite adsorbents with enhanced adsorption capabilities, achieved through complementary chemical compositions and pore-structure optimization. Ma et al. [111] mixed EMR with serpentine and calcined the mixture at 800 °C for 2 h to prepare a composite adsorbent with a specific surface area of 11.998 $m^2 \cdot g^{-1}$. The adsorption capacities of this adsorbent for Cd^{2+} and Pb^{2+} reached 98.05 $mg \cdot g^{-1}$ and 565.81 $mg \cdot g^{-1}$, respectively. Jiang et al. [112] prepared a non-sintered adsorbent composite granular filler (CGF), using CFA, steel slag, and desulfurized gypsum (DG) as raw materials, cement as an activator and binder, and hydroxypropyl methylcellulose (HPMC) as a water-retaining agent dispersant, through roll-forming. To prevent the expansion and cracking of CGF, the formed adsorbent underwent 7 days of hydrothermal curing, followed by 21 days of natural curing. The CGF exhibits an approximately elliptical shape with an average diameter of about 5 mm; a bulk density of 0.928–1.08 $g \cdot cm^{-3}$; a filling porosity of $\geq$30%; a specific surface area of $\geq 1.915 \times 10^5$ $cm^2 \cdot g^{-1}$; a water absorption ratio of $\geq$12.97%; and an average pore size of $\geq$9.32 nm. Qi et al. [113] used CFA from a coal-fired power plant and sludge from a wastewater-treatment plant as the main feedstocks for an adsorbent. The sludge supplied iron, while the CFA supplied carbon. The resulting adsorbent is a magnetic iron–carbon composite that can be rapidly separated and recovered under an applied magnetic field. Its specific surface area is 228.65 $m^2 \cdot g^{-1}$, pore volume is 0.24 $cm^3 \cdot g^{-1}$, and average pore diameter is 4.22 nm, indicating a predominantly mesoporous material. Zhan et al. [41] mixed bentonite with steel slag powder in a certain proportion, added Na_2CO_3 and DW, and obtained the composite adsorbent BSC after granulation and calcination.

3.4.2. Inorganic Solid Waste–Biomass Composites

Mixing IISWs with biomass and then calcining it allows the biomass to serve as a carbon source or to improve the adsorbent's structure. Feng et al. [114] mixed red mud, dried urban sludge, lignin, and chitosan in a certain mass ratio, followed by calcination to obtain a lignin-modified spontaneous magnetic sludge-based biochar (LC@SRBC) adsorbent. The LC@SRBC adsorbent has a rough surface and possesses mesoporous and microporous structures. Wei et al. [115] developed an EMR–biochar (EB) composite through one-step pyrolysis using a mixture of EMR and distillers grains. The metal oxides in EMR facilitate co-pyrolysis onto biochar, modifying its physicochemical properties and enhancing adsorption capacity. At elevated temperatures, cellulose-like components in the lees degrade progressively, releasing volatile compounds and promoting pore formation. Liu et al. [116] used phosphogypsum to prepare a distillers grains-modified engineered biochar (DGMC600) composite, which could remove fluoride (F^-) and arsenic (As^{5+}) from water. As a calcium-rich material, phosphogypsum undergoes Ca^{2+} modification that transforms micropores into macropores, significantly increasing pore volume and specific surface area. When co-thermally pyrolyzed with biomass feedstock, phosphogypsum alters the functional groups and surface charge of biochar, thereby enhancing its pollutant adsorption capacity. This innovative approach of chemical activation and surface functionalization effectively increases the density of active binding sites. Wang et al. [117] prepared TiO_2-loaded phosphogypsum-modified biochar (TYBC) by mixing phosphogypsum with TiO_2 and rapeseed straw in a weight ratio of 2:1:1. The mixture was carbonized under a nitrogen

atmosphere and heated to a specified temperature, then maintained for 30 min. The modification significantly increased the specific surface area of the original biochar, attributed to the formation of Ca–O and Ti–O bonds during pyrolysis. Jiang et al. [118] prepared a phosphogypsum-modified biochar composite (PMBC) via one-step pyrolysis using phosphogypsum, wood chips, and distillers grains as raw materials. The moisture content of the PMBC was reduced, and many fine particles appeared on the surface. The introduction of phosphogypsum promoted the formation of functional groups on the PMBC surface.

By forming composite or hybrid adsorbents from solid waste and other components, chemical synthesis can also enhance adsorbent performance. Li et al. [119] synthesized white spherical solid particles of RMZA-CS with diameters ranging from 1 mm to 2 mm using red mud and chitosan as raw materials. RMZA-CS is a composite material of zeolite and biomass chitosan, with a BET specific surface area of 11.38 $m^2 \cdot g^{-1}$. The preparation process of RMZA-CS is shown in Figure 5.

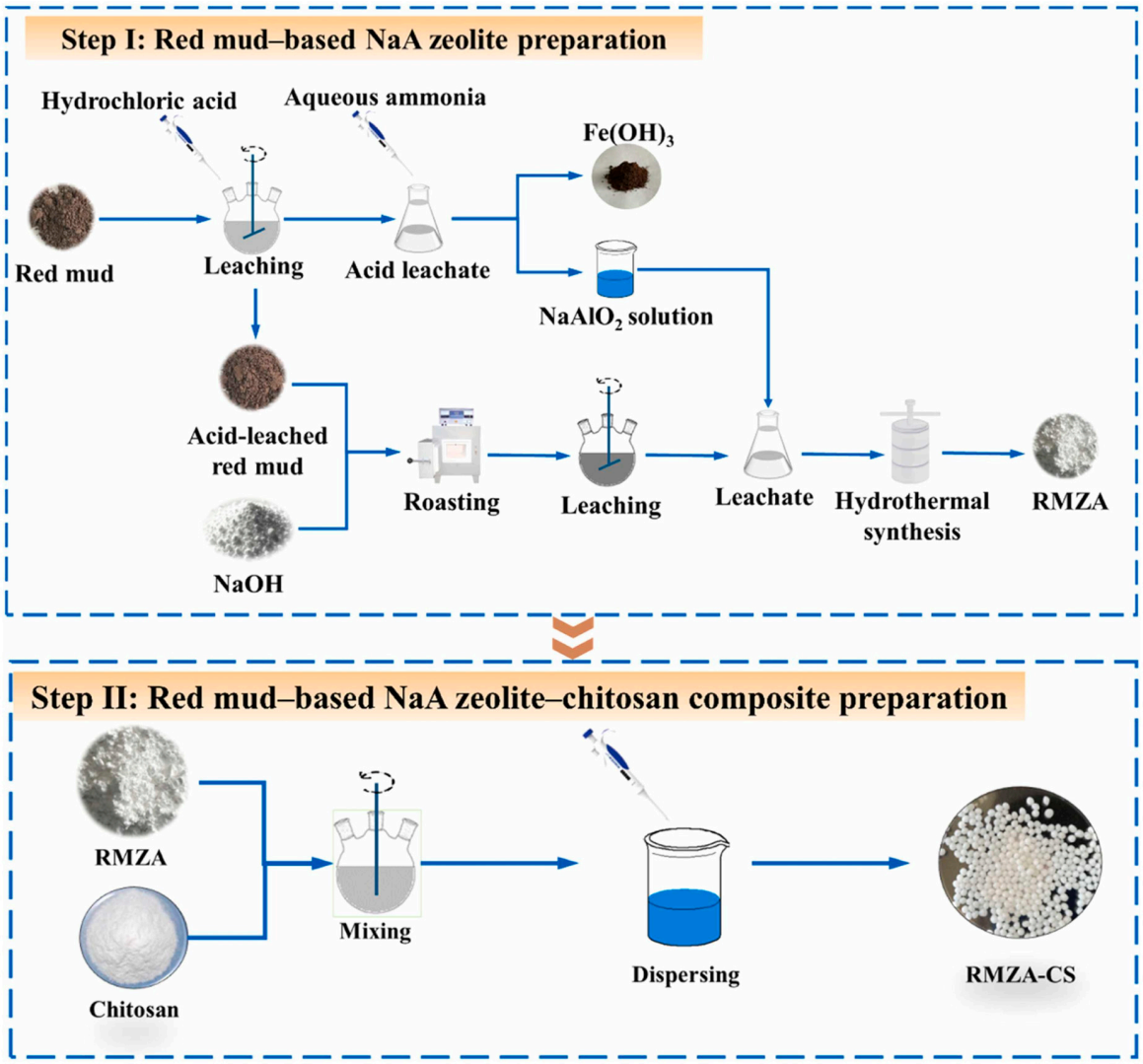


Figure 5. Overview of the synthetic pathways for RMZA-CS. Reprinted with permission from reference [119]. Copyright 2025, Elsevier.

3.5. Potential Environmental Benefits

The utilization of IISWs in the preparation of adsorbents offers innovative solutions for environmental pollution control, resource conservation, and energy efficiency. This

approach not only constitutes an effective strategy for environmental management but also represents a critical pathway toward advancing sustainable development.

(1) Environmental pollution control

The utilization of IISWs for the preparation of adsorbents represents a dual-benefit strategy that not only mitigates the environmental pollution caused by the disposal of these wastes but also provides cost-effective materials for the removal and immobilization of contaminants from water, air, and soil. On the one hand, pollutants such as heavy metals and ammonia nitrogen in IISWs are removed or stabilized during the adsorbent preparation process, thereby reducing the discharge of contaminants from the wastes themselves. On the other hand, the obtained adsorbents can eliminate or immobilize pollutants like heavy metals and organic compounds in applications such as wastewater treatment, exhaust gas control, and soil pollution remediation, effectively controlling environmental pollution [6]. Furthermore, IISWs play a significant role in carbon emission reduction. Li et al. [120] developed an EMR treatment technology that enables CO_2 mineralization by directly utilizing EMR as a feedstock and ammonia as a recyclable agent, thereby mitigating carbon emissions from the electrolytic manganese industry. Specifically, this process can solidify 0.16 tons of CO_2 for every 1 ton of EMR processed. Thus, this approach transforms an environmental liability into a functional resource, closing the loop in industrial material flows and promoting sustainable environmental management.

(2) Resource conservation

The conversion of IISWs into functional adsorbents aligns with circular economy principles by transforming discarded resources into valuable materials. This process reduces landfill burdens and production costs while utilizing inherent components to create high-value adsorption materials [114]. These waste-derived adsorbents simultaneously enable the recovery of valuable pollutants from wastewater and exhaust streams, including heavy metals and nutrients. This dual benefit of waste valorization and resource recovery offers scalable, eco-friendly solutions for pollution control and sustainable resource management across various industries. The approach demonstrates how industrial byproducts can be repurposed to address environmental challenges while promoting resource efficiency. Closing material loops represents a practical implementation of circular economy concepts in pollution treatment and waste management applications.

(3) Energy conservation

IISWs play a non-negligible role in energy conservation, offering dual environmental and economic benefits through innovative material repurposing. The utilization of such wastes significantly reduces energy consumption and operational costs while promoting circular economy principles. For instance, slag-derived zeolite synthesized from BFS demonstrates remarkable cost-effectiveness, with a production cost of approximately \$1.50/kg. This technology generates an economic benefit of about \$302.14 per ton of BFS, highlighting its potential for large-scale application [121].

4. Applications of IISW-Derived Adsorbents

IISW-derived adsorbents have been widely used for various pollution control purposes, including the adsorption of organic and inorganic pollutants from contaminated water, as well as the control of air and soil pollution.

4.1. Adsorption of Pollutants in Aqueous Solutions

Wastewater pollution has become a global challenge. The bioaccumulation of pollutants adversely affects organisms, disrupts aquatic ecosystem balance, and causes severe

mutagenic and carcinogenic effects. Water pollutants are broadly classified into inorganic and organic pollutants. Wastewater is characterized by its large volume. Adsorbents produced from IISWs are low-cost, helping reduce treatment costs.

4.1.1. Adsorption of Inorganics

Inorganic pollutants primarily include metal ions, NH_4^+-N, and non-metallic inorganic compounds such as sulfates and phosphates. Industries such as electroplating, metallurgy, and mining are major sources of heavy metal ion pollution, with common examples including Cd(II), Cu(II), Pb(II), and Ni(II) [122]. Even at low concentrations, these inorganic pollutants exhibit high toxicity, carcinogenicity, and non-biodegradability.

(1) Metal ions and NH_4^+-N

Heavy metal ions are extremely dangerous environmental pollutants due to their high toxicity, carcinogenicity, and potential for bioaccumulation [123]. The acceleration of industrialization has led to a large amount of wastewater discharge, especially from mining, smelting, electroplating, and pigment manufacturing, all of which are rich in heavy metal ions. If this kind of wastewater is discharged into the environment untreated, it will cause serious harm to the environment and human health. Inorganic pollutants such as Cr(VI) and As(V) cannot be eliminated through chemical methods. Therefore, an alternative approach to mitigate their harmful effects is to reduce inorganic pollutants in water resources through adsorption, thereby eliminating their pollution.

IISWs-derived adsorbents offer environmental protection and economic benefits, effectively removing metal ions from water bodies and providing a low-cost, green, and feasible solution for water remediation. Agrawal et al. [124] used sea nodule residue(SNR), fly ash, and red mud as adsorbents to adsorb Cu^{2+}. Under optimized experimental conditions, the adsorption capacity was 19.65 $mg \cdot g^{-1}$ for SNR, 1.98 $mg \cdot g^{-1}$ of fly ash, and 2.28 $mg \cdot g^{-1}$ of red mud. Li et al. [12] demonstrated that the RML-NaA zeolite exhibited a maximum adsorption capacity of 91.49 $mg \cdot g^{-1}$ for Ni^{2+}, with stable performance after five adsorption–desorption cycles, showing significant potential for industrial wastewater treatment. The MRM adsorbent prepared by Zhong et al. [6] achieved a maximum adsorption capacity of 8.22 $mmol \cdot g^{-1}$, with Ni-loaded MRM demonstrating high stability. Ibsaine et al. [125] found that the lithium slag-derived zeolite Na-P1 demonstrates excellent adsorption capacity for Ca^{2+} and NH_4^+ ions. At 58 °C, it effectively reduces water hardness to 18 $mg \cdot L^{-1}$. Additionally, Na-P1 zeolite shows high maximum adsorption capacities for Cd^{2+} (138 $mg \cdot g^{-1}$), Ce^{3+} (209 $mg \cdot g^{-1}$), Cr^{3+} (56.2 $mg \cdot g^{-1}$), and Cu^{2+} (60.5 $mg \cdot g^{-1}$), and NH_4^+ (51.0 $mg \cdot g^{-1}$). The EMR-derived zeolite prepared by Li et al. [16] exhibited equilibrium adsorption capacities of 29.85 $mg \cdot g^{-1}$ for Mn^{2+} and 47.39 $mg \cdot g^{-1}$ for NH_4^+, with Mn^{2+} adsorption reaching equilibrium within 200 min. The adsorption rate of NH_4^+ ions was significantly faster than that of Mn^{2+}, achieving equilibrium within 15 min. Xu et al. [126] investigated the adsorption of Tl(I) in Tl(I)-containing wastewater using iron-based water treatment residue (Fe-WTR) and aluminum-based water treatment residue (Al-WTR) as adsorbents from a municipal water treatment plant. The results demonstrated that the adsorption capacity of both Fe-WTR and Al-WTR showed a positive correlation with pH. Fe-WTR exhibited superior removal efficiency for Tl(I) compared to Al-WTR. Notably, Tl(I) adsorbed by Fe-WTR predominantly existed in reduced form, whereas Al-WTR adsorbed Tl(I) mainly in acid-extractable and reduced states. Qi et al. [113] prepared an adsorbent using Fenton sludge and fly ash as raw materials, which exhibited good adsorption performance for Cr(VI) in aqueous solutions. Under the conditions of T = 273.15 K, pH = 10, t = 1200 min, and an initial Cr(VI) concentration (C_0) = 100 $mg \cdot L^{-1}$, the removal efficiency of Cr(VI) exceeded 80%. Chen et al. [103] utilized NiO@γ-Al_2O_3 sludge composite materials for Cd^{2+} adsorption. At the optimal dose of 1.5 $g \cdot L^{-1}$, the Cd^{2+} removal efficiency reached 99.9%.

(2) Anions

The inorganic salts in urban sewage and industrial wastewater are mainly sulfate, arsenate, and phosphate. The primary sources of phosphate are the over-exploitation of phosphate rock resources and the excessive use of phosphate fertilizers. Phosphorus is one of the main factors contributing to water eutrophication. The discharge of urban sewage and industrial wastewater into water bodies not only affects water quality but also causes significant economic losses.

IISWs-derived adsorbents were prepared for the adsorption of phosphate from wastewater, providing a new approach to the high-value utilization of solid waste and the treatment of water eutrophication. Ge et al. [127] demonstrated that the adsorbent prepared from sewage sludge and municipal solid waste incineration bottom ash exhibited exceptional phosphate removal efficiency. The synthesized adsorbent maintained a nearly constant adsorption capacity of approximately 490.6 $mg \cdot kg^{-1}$ for phosphate across a pH range of 3 to 10. Sousa et al. [128] conducted physical and chemical property analyses on seven drinking water treatment sludges (DWTSs) with varying ash content, followed by adsorption tests under neutral pH conditions. Six of these DWTSs demonstrated phosphoric acid (PO_4^{3-}) adsorption capacity ranging from 6.7 $mg \cdot g^{-1}$ to 44.1 $mg \cdot g^{-1}$. The study revealed that aluminum content was not a critical parameter in the adsorption process. Instead, the pH at the zero charge point proved to be the decisive factor. The predominant positive surface charge on DWTSs facilitated the adsorption of anionic species such as phosphate ions. Liu et al. [101] applied an in situ Fe-Al adsorbent to arsenate removal from wastewater. The maximum adsorption capacity of As(V) at 35 °C is 168.04 $mg \cdot g^{-1}$, which is higher than that of some existing adsorbents. Under optimal conditions, the removal efficiency of As(V) exceeded 99%, with the As(V) concentration in the adsorbed solution remaining below 0.1 $mg \cdot L^{-1}$, meeting China's comprehensive wastewater discharge standards. Ning et al. [82] investigated the F^- removal capability of Fe-WTR in aqueous solutions. The Langmuir model calculated a theoretical maximum adsorption capacity of 16.09 $mg \cdot g^{-1}$. Fe-WTR reached equilibrium within 1.5 h for F^- adsorption. The adsorption capacity remained stable across a pH range of 4–9, indicating that Fe-WTR is adaptable to a wide range of application environments.

4.1.2. Adsorption of Organics

Organic pollutants mainly include organic dyes, microplastics, emerging persistent organic pollutants, and antibiotics.

(1) Organic dyes

Dye-intensive manufacturing processes generate substantial colored wastewater containing toxic substances such as Congo red, methylene blue, and rhodamine B. Notably, Congo red—a benzene compound anionic dye classified as both carcinogenic and mutagenic—causes severe irritation to the skin, reproductive system, and eyes. While methylene blue is alkaline and less toxic, it can still cause significant irritation upon contact with the skin or eyes. As a water-soluble dye, untreated rhodamine B discharged into natural water bodies leads to water discoloration, reduced light transmittance, inhibition of aquatic plant photosynthesis, and disruption of aquatic ecosystems. Li et al. [31] investigated the adsorption of methylene blue by EMR-derived zeolite EMRZ in dye-containing solutions. The adsorption capacity of methylene blue increased with rising pH, from 13.78 $mg \cdot g^{-1}$ to 37.05 $mg \cdot g^{-1}$ when pH rose from 2.0 to 12.0. Within a broad pH range (4.0–12.0), EMRZ exhibited surface negative charges, enabling methylene blue cations to achieve higher adsorption capacity at elevated pH levels. Xie et al. [129] immobilized flake-shaped NiOOH on activated red mud to obtain an ARM/NiOOH adsorbent for wastewater treatment, demonstrating its effectiveness in removing organic dyes. The

ARM/NiOOH adsorbent, characterized by high specific surface area and porosity, provided abundant active sites for Congo red, significantly enhancing Congo red removal efficiency. An et al. [130] utilized zinc-aluminum silicate (ZAS) to modify waste granular red mud (GRM), forming a ZAS/GRM adsorbent that provides active sites for Congo red, thereby significantly enhancing Congo red removal efficiency. Jankowska et al. [100] employed 3-aminopropyltrimethoxysilane (APTMS) and 3-aminopropyltriethoxysilane (APTES) for amino-functionalization to modify MCM-41, which was subsequently used for the adsorption and removal of azo dyes (sunset yellow FCF and tartrazine) in water. The APTMS-modified MCM-41 exhibited the highest adsorption performance, achieving an adsorption capacity of 531 $mg \cdot g^{-1}$ for sunset yellow FCF and 360 $mg \cdot g^{-1}$ for tartrazine. Cao et al. [47] utilized modified red mud MRM-PS to adsorb rhodamine B dye from wastewater. The study demonstrated that the adsorption capacity reached its maximum at pH 1 (59.37 $mg \cdot g^{-1}$) and that adsorption kinetics were rapid, with equilibrium achieved within 10 min.

(2) Microplastics

Beyond dyes, organic pollutants include microplastics—plastic particles formed through improper environmental discharge, UV exposure, weathering, and physical abrasion. These microplastics can adsorb toxic contaminants such as polycyclic aromatic hydrocarbons, polychlorinated biphenyls, and heavy metals via hydrophobic interactions, electrostatic forces, and hydrogen bonding. Their environmental accumulation, transport, and interactions with other toxic pollutants pose serious ecological risks. LC@SRBC, a red mud-derived adsorbent developed by Feng et al. [114], exhibited excellent adsorption performance for polystyrene nanoplastics (PSNPs) in wastewater. In a 100 $mg \cdot L^{-1}$ PSNPs solution, it achieved a removal efficiency of 97.87%.

(3) Emerging persistent organic pollutants

Perfluoro-and polyfluoroalkyl substances (PFAS) are a class of emerging persistent organic pollutants. Due to their high stability, economically effective remediation of PFAS pollution through chemical or biochemical degradation is challenging. Zhang et al. [131] investigated the adsorption removal of perfluorooctanoic acid (PFOA) and perfluorooctane sulfonic acid (PFOS) from water using Al-WTR. The adsorption isotherm model revealed that at pH 3.0, the maximum adsorption capacities for PFOA and PFOS on Al-WTR were 0.232 $mg \cdot g^{-1}$ and 0.316 $mg \cdot g^{-1}$, respectively. Lower pH enhances the adsorption process, resulting in faster rates and higher capacities. The irreversible nature of Al-WTR adsorption makes it an ideal adsorbent for removing PFOA and PFOS from solution.

(4) Antibiotics

Antibiotic contamination in aqueous solutions can readily induce drug resistance genes, disrupt ecological balance, and pose health risks to humans through the food chain. Solid waste-derived adsorbents offer an economically viable and environmentally friendly new approach for water pollution control. Sousa et al. [132] investigated the removal capacity of DWTS for antibiotics in water. At 40 °C, the maximum adsorption capacity of DWTS for trimethoprim (TMP) in a single solution was 26.8 $mg \cdot g^{-1}$. For sulfamethoxazole (SMX) in a single solution, the monolayer adsorption capacity calculated using the Langmuir model was 36.7 $mg \cdot g^{-1}$. The oxygen-containing functional groups in DWTS participated in the adsorption mechanisms of the tested antibiotics through hydrogen bonding. Wang et al. [117] utilized the prepared biochar adsorbent TYBC450 to remove residual ofloxacin (OFL) from the environment. The adsorption efficiency of TYBC450 for OFL was 88.16%, with an adsorption capacity of 1.75 $mg \cdot g^{-1}$.

4.2. Air Pollution Control

Air pollution is a significant environmental issue that cannot be ignored in modern industry. Adsorbents derived from IISWs can adsorb typical air pollutants, including nitrogen oxides (NO_x), COS, volatile organic compounds (VOCs), and carbon dioxide (CO_2).

4.2.1. Adsorption of Gaseous Pollutants

NO_x is a reactive gas mainly consisting of nitrogen and oxygen, primarily originating from high-temperature combustion processes. NO_x poses significant harm to humans and organisms and has become a key focus of air pollution control efforts. Apeksha et al. [133] investigated the application of solid waste as a potential adsorbent for reducing NO_x in diesel engine exhaust after plasma discharge and ozone mixed pretreatment. Wastes such as red mud, CFA, and foundry sand were processed to form mesoporous structures. Plasma pretreatment resolved the issue of nitric oxide (NO) adsorption difficulty, while the solid waste adsorbent efficiently captured oxidized nitrogen dioxide (NO_2). The combined cascade process achieved a denitrification efficiency of 90–95%.

COS, primarily originating from industrial sources, is predominantly found in reducing atmospheres. COS promotes the formation of sulfate aerosols in the air, posing hazards to the environment, animals, and plants. Plants can absorb it and exhibit neurotoxicity to animals. Many factories use various types of gas as fuel, and COS ultimately converts to sulfur dioxide (SO_2), which is released into the atmosphere and is detrimental to achieving ultra-low emissions. Zhou et al. [28] investigated the optimal process parameters for COS adsorption purification using the adsorbent. Under optimal conditions, the new adsorbent achieved an adsorption efficiency exceeding 95%, with a COS adsorption capacity of 63.56 $mg \cdot m^{-3}$.

As typical air pollutants, VOCs not only contribute to atmospheric pollution but can also enter the human body through multiple pathways, causing a series of pathological changes. Sun et al. [90] developed a ZSM-5 zeolite using CGS desilication liquid as the primary silicon and sodium source for VOCs adsorption. In static adsorption experiments, the ZSM-5 zeolite prepared under optimal conditions exhibited saturated adsorption capacities of 69.98 $mg \cdot g^{-1}$ for benzene, 68.74 $mg \cdot g^{-1}$ for toluene, 118.85 $mg \cdot g^{-1}$ for p-xylene, and 95.85 $mg \cdot g^{-1}$ for butyl acetate. This method facilitates high-value utilization of silicon resources from IISWs and provides a novel approach to address air pollutant control through solid waste utilization.

Other substances that need to be absorbed in the air include water vapor and iodine [134,135]. Chen et al. [92] investigated the adsorption of water vapor using lithium slag-based zeolite NaX-1, demonstrating a maximum adsorption capacity of 0.3208 $kg \cdot kg^{-1}$, which is close to the commercial standard of 0.3303 $kg \cdot kg^{-1}$. Fotsop et al. [135] investigated the iodine removal capacity of zeolites. The undoped zeolite (Zeo-4A-Na) exhibited an experimental equilibrium capacity about 360 $mg \cdot g^{-1}$, while zeolites doped with Bi, Zn, and Ag showed equilibrium capacities of 620 $mg \cdot g^{-1}$, 710 $mg \cdot g^{-1}$, and 780 $mg \cdot g^{-1}$, respectively.

4.2.2. Carbon Dioxide Capture

The increase in greenhouse gas (GHG) emissions, particularly CO_2, has led to climate change and global warming. Among various technologies, adsorption technology using solid adsorbents has shown great potential for reducing carbon emissions and achieving a sustainable future for the planet. The adsorbent developed by Zhang et al. [79] demonstrated optimal high-temperature adsorption performance at 700 °C in a pure CO_2 atmosphere, achieving a remarkable adsorption capacity of 0.681 $g \cdot g^{-1}$—1.58 times that of commercial CaO. Liang et al. [136] demonstrated that red mud-derived solid amine

adsorbents showed significantly higher CO_2 adsorption capacity compared to raw red mud. The adsorption performance was notably influenced by both the type and loading amount of organic amine. A comparative analysis of various organic amine variants revealed that the most effective adsorbent achieved a maximum CO_2 adsorption capacity of 29.3399 $mg \cdot g^{-1}$. Li et al. [137] discovered that red mud exhibits a synergistic effect of "enhanced adsorption + catalytic desorption" on CO_2. The adsorption phase enhances CO_2 capture capacity by optimizing physical mass transfer and regulating the chemical environment. The enhancement mechanisms of red mud particles for CO_2 absorption and desorption are shown in Figure 6.

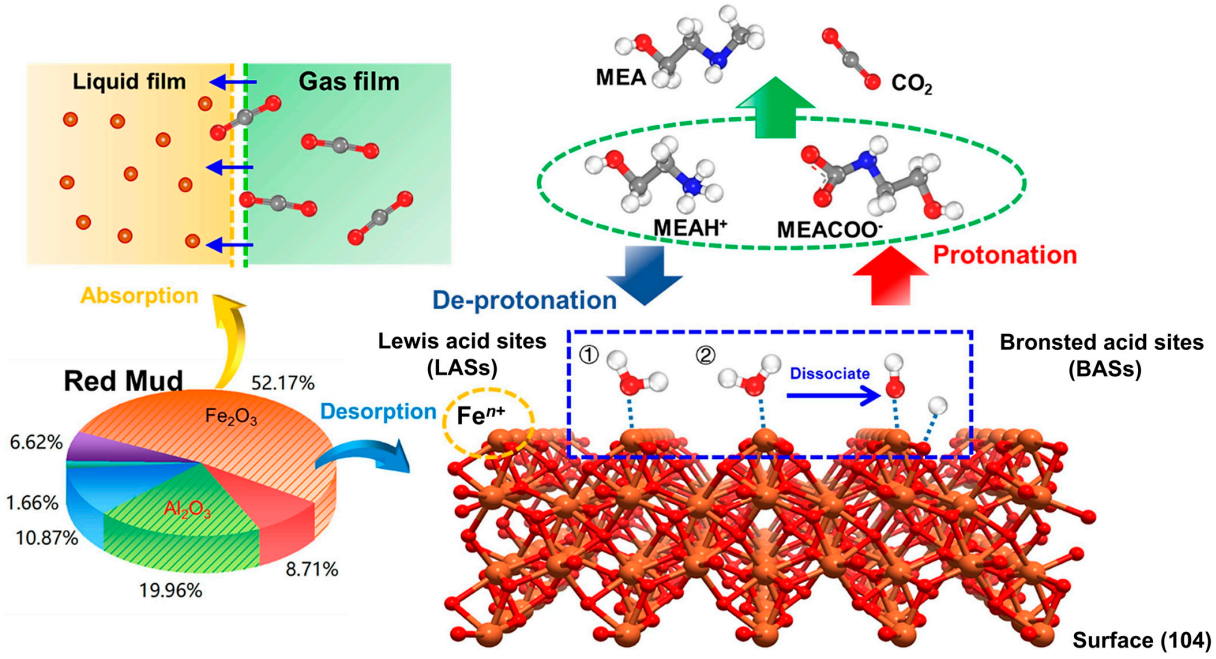


Figure 6. Enhancement mechanisms of red mud particles for CO_2 absorption and desorption. Reprinted with permission from reference [137]. Copyright 2023, Elsevier.

4.3. Soil Pollution Remediation

Heavy metal-contaminated soils in industrial settings contain elements commonly toxic to organisms and to aerobic/anaerobic processes, including arsenic, cadmium, chromium, copper, lead, mercury, nickel, selenium, and zinc. The remediation of such soils aims to mitigate their adverse effects on human health and the environment while supporting ecosystem restoration and biodiversity conservation. Currently, the solid waste-derived adsorbents used in the research of soil remediation are red mud-derived and EMR-derived.

Red mud, characterized by its high pH and composition of iron oxide, aluminum oxide, and hydroxides, is an ideal material for remediation and has significant potential as a soil environmental restoration agent. Xu et al. [138] investigated the effects of red mud-derived passivators on Cd transformation, photosynthetic characteristics, and Cd accumulation in edible amaranth in acidic Cd-contaminated soils. The results demonstrated that red mud exhibited strong Cd adsorption capacity in aqueous solutions at approximately 35 °C and pH 9. After the red mud application, the increase in organic matter led to reduced effective Cd content in soil aggregates, thereby promoting plant growth. Following the waste treatment principle, Liang et al. [27] modified red mud using a coconut shell thermal reduction method for Cr(VI)-contaminated soil remediation. The modified red mud, with its abundant porous structure and reduced iron (zero-valent iron), facilitates Cr(VI) remediation through adsorption and redox reactions. Remarkably, it achieved 100% efficiency in reducing Cr(VI) in soil. This reduction likely occurs because the zero-valent

iron (ZVI) in the modified red mud adsorbs and reduces Cr(VI) during the mixing process. Chen et al. [139] synthesized a low-carbon curing agent (RAS) using red mud, GGBS, calcium carbide residue (CCR), and phosphogypsum for stabilization of Cd-contaminated soil. After 14 days of stabilization, the leaching rate of Cd in the stabilized soil containing 10% RAS was below the leaching threshold of 1 $mg \cdot L^{-1}$.

EMR contains high concentrations of metal elements such as Fe, Mn, Ca, and Mg. These elements can be converted into stable metal (hydrogen) oxides after pyrolysis, serving as key carriers for heavy metals in fixed soils. Wei et al. [140] utilized an EB to remediate soils co-contaminated with antimony and arsenic. Through column leaching experiments, they investigated the immobilization effects of EB on these metals. Results demonstrated that the 4 wt% EB treatment reduced accumulated Sb and As concentrations in leachate by 29.21–55.65% and 53.51–68.95%, respectively, compared to the control group. Given EB's superior specific surface area and pore volume compared to other biochar materials, its Sb and As immobilization mechanism likely stems from these advantages. Energy-dispersive X-ray spectroscopy (EDS) analysis revealed 1.32% As and 0.28% Sb adsorbed on the immobilized EB, confirming their surface fixation in the soil.

4.4. Summary, Risks, and Challenges

4.4.1. Summary of Application Performance for IISWs-Derived Adsorbents

IISWs-derived adsorbents, as a key technology for "waste-to-waste" treatment, demonstrate broad application prospects in wastewater treatment, air pollution control, and soil remediation due to their advantages of low-cost raw materials, flexible preparation processes, and excellent environmental compatibility [123]. As can be seen from the data above, IISWs-derived adsorbents exhibit excellent adsorption performance for various pollutants. The maximum adsorption capacity and adsorption conditions of IISWs-derived adsorbents are included in Supplementary Materials Table S1. It can also be concluded that each of these adsorbents has its own characteristics, including strengths and weaknesses, making them suitable for different application scenarios. A comparison of application fields and characteristics for IISWs-derived adsorbents is presented in Supplementary Materials Table S2.

4.4.2. Risks and Challenges

The preparation of adsorbents from inorganic industrial solid waste is a promising development direction, beneficial for both solid waste treatment and the advancement of adsorption and separation technologies. However, the existing literature seldom addresses the associated negative impacts, including secondary pollution during the use of adsorbents, potential contamination risks in the preparation process, and application challenges resulting from complex manufacturing procedures. Due to the inherent properties of inorganic pollutants, such as high alkalinity and elevated heavy metal content, uncontrolled release during either the application or preparation of adsorbents can lead to their dispersion into the environment [6]. This may result in adverse effects that are difficult to remediate, necessitating proactive prevention measures. During the preparation and application of adsorbents, the complexity of the processes driven by environmental and technical requirements also poses challenges for the "waste-to-waste" treatment strategy. A simplistic assumption of a win-win outcome may not always achieve the desired results, and improper handling can instead lead to a lose-lose situation. The identification of leaching toxicity in treated EMR conducted by Li et al. [16] and Wang et al. [76] demonstrated that its leaching toxicity complies with relevant environmental protection standards. However, the long-term environmental impact risks of adsorbents derived from industrial solid waste still require further investigation to assess their ecological safety and sustainability in practical applications fully. Additionally, concerns from both the

government and the public regarding the risk of environmental pollution spread from inorganic industrial solid waste deserve serious attention. The use of IISWs in adsorbents still faces potential risks related to governmental policy and public opinion. In summary, this strategy still faces numerous challenges. Greater efforts are needed from researchers, enterprises, governments, and the public to advance related initiatives.

5. Adsorption Behaviors and Mechanisms

Adsorption processes involve complex physicochemical behaviors and mechanisms, which collectively contribute to distinct characteristics. In adsorption research, it is common to employ an integrated approach that combines adsorption kinetics, adsorption isotherms, thermodynamic analysis, computational chemistry, and analytical instrumentation measurements. The results of these diverse techniques can be integrated to provide a more comprehensive understanding of the adsorption process.

5.1. Physicochemical Behaviors of Adsorption Processes

Adsorption kinetics, isothermal adsorption, and thermodynamic studies are fundamental for characterizing the rate, capacity, and energy changes in adsorption processes, thereby providing critical insights into the underlying mechanisms, such as mass transfer, surface interactions, and process spontaneity. These studies typically involve collecting data experimentally, which is then processed using physicochemical equations to derive the desired parameters.

5.1.1. Adsorption Kinetics

The typical diffusion and adsorption process of an adsorbent involves the following sequential stages [101,141]. (1) Bulk diffusion: The adsorbate migrates from the bulk solution to the boundary layer surrounding the adsorbent particles. (2) Film diffusion (liquid-film diffusion/external diffusion): The adsorbate is transported across the boundary layer to the external surface of the adsorbent. (3) Intra-particle diffusion (pore diffusion/internal diffusion): The adsorbate penetrates the pores of the adsorbent particles, reaching internal surfaces where it distributes in an adsorbed state. (4) Adsorbate attachment (adsorption): The adsorbate attaches to active adsorption sites via chemical and/or physical interactions. This multi-step mechanism is influenced by factors such as adsorbent porosity, solution concentration, temperature, and the chemical nature of both adsorbent and adsorbate, collectively determining the overall adsorption kinetics and efficiency.

The study of adsorption kinetics typically involves investigating the effect of contact time on adsorption capacity, followed by fitting the data to kinetic models. Through the analysis of the dynamic models, the diffusion rate and the rate-determining steps of adsorption can be obtained. Common kinetic models include pseudo-first-order, pseudo-second-order, Elovich, liquid film diffusion, and intra-particle diffusion models. Han et al. [142] used magnesium-aluminum layered double oxide (MgAl-LDO) prepared from aluminum slag to remove Cu^{2+} and Pb^{2+} from wastewater. Kinetic studies showed that the adsorption followed a pseudo-second-order model, indicating that chemical adsorption was the dominant process. Through the study of pseudo-first-order, pseudo-second-order, Elovich, liquid-film diffusion, and intra-particle diffusion models, Chen et al. [143] found that the rate-limiting steps for the adsorption of Cd^{2+} from water by the biomass-derived adsorbent are mainly film diffusion and intraparticle diffusion. Gao et al. [144] employed pseudo-first-order and pseudo-second-order kinetic models to analyze the adsorption process. Their study revealed that the pseudo-second-order model yielded higher correlation coefficients (R^2 = 0.96–0.99), with the calculated equilibrium adsorption capacity (q_e) closely matching experimental values. The model incorporates multiple mechanisms, including liquid-film

diffusion, surface adsorption, and intraparticle diffusion, indicating that the adsorption process involves complex chemical interactions rather than simple physical diffusion. This finding provides kinetic evidence supporting chemical adsorption mechanisms such as "ligand exchange".

5.1.2. Adsorption Isotherms

Adsorption isotherms provide critical insights into the distribution of adsorbate molecules on an adsorbent, offering valuable references for analyzing adsorption systems. The Langmuir, Freundlich, and Temkin adsorption isotherms are commonly used to describe isothermal adsorption processes. The Langmuir isotherm assumes homogeneous adsorption on a single-layer surface, while the Freundlich isotherm describes adsorption occurring on heterogeneous surfaces. The Temkin isotherm accounts for heterogeneous surfaces and exhibits a linear reduction in adsorption heat. Finally, the D-R isotherm helps determine whether the adsorption process is physical or chemical.

The study of adsorption isotherms typically involves investigating the effect of initial adsorbate concentration on adsorption capacity at a constant temperature, followed by fitting the data to isothermal adsorption models. In the Ni^{2+} adsorption experiment, the Langmuir isotherm provided the most accurate fit for the equilibrium adsorption data of MRM prepared by Zhong et al. [6], indicating that the adsorption of Ni^{2+} by MRM occurs through monolayer adsorption. Li et al. [31] investigated the adsorption isotherm of methylene blue on EMRZ. The Langmuir isotherm demonstrated excellent linear fit, indicating that methylene blue adsorption on EMRZ follows a monolayer mechanism with uniform sites and no intermolecular interactions. The Freundlich isotherm showed a correlation coefficient (R^2) ranging from 0.8279 to 0.9521, significantly lower than that of the Langmuir isotherm, suggesting that the heterogeneous surface adsorption hypothesis is not applicable.

5.1.3. Adsorption Thermodynamics

Adsorption thermodynamics typically involves changes in enthalpy (ΔH), entropy (ΔS), and Gibbs free energy (ΔG), providing insights into the thermodynamic properties and interaction mechanisms of adsorption processes. ΔH, ΔS, and ΔG reflect heat exchange and energy efficiency, alterations in the disorder of systems, and the overall spontaneity and feasibility of adsorption, respectively.

The study of adsorption thermodynamics primarily involves calculating ΔH, ΔS, and ΔG, with the resulting values used to determine the thermodynamic nature of the adsorption process. The adsorption capacities of the complex EB prepared by Wei et al. [115] for As and Sb increased with rising temperature. The ΔH values for EB's adsorption of As(III), As(V), Sb(III), and Sb(V) are positive, indicating an endothermic process. The positive ΔS values suggest highly random adsorption at the solid–liquid interface for As(III, V) and Sb(V). Conversely, the negative ΔS value for Sb(III) adsorption indicates reduced randomness between EB and Sb(III) solution. Within the temperature range of 15–35 °C, the ΔG values for EB's adsorption of As(III), As(V), Sb(III), and Sb(V) are all positive, demonstrating that the adsorption process is non-spontaneous. Duan et al. [121] investigated the thermodynamics of CO_2 adsorption by BFS-derived zeolites. Within the temperature range of 313 K to 373 K, the ΔG remained negative and became less negative with increasing temperature, indicating a reduced tendency for spontaneous CO_2 adsorption. The ΔH was -18.1100 kJ·mol^{-1}, confirming an exothermic process in which elevated temperatures hinder CO_2 adsorption. The ΔS of -0.0452 kJ·mol^{-1}·K^{-1} suggests decreased disorder at the adsorption interface, implying that the CO_2 adsorption process is energetically stable and well-ordered.

5.2. Mechanisms of Adsorbate–Adsorbent Interactions

Elucidating the interaction mechanisms between adsorbates and adsorbents lies at the core of exploring adsorption performance and optimizing adsorbent design, with the involved action forces and micro-processes identifiable via a combination of computational simulations and analytical instrument characterization. The intrinsic interaction mechanisms include hydrogen bonding, electrostatic attractions, π–π stacking, cation exchanges, and surface complexations, which can drive adsorption jointly or independently. Quantum chemistry and molecular dynamics (MD) simulations are the main computational approaches for revealing adsorption configurations, the nature of active sites, and dynamic adsorption processes at the molecular and electronic levels. Meanwhile, Fourier-transform infrared spectroscopy (FTIR), X-ray diffraction (XRD), X-ray photoelectron spectroscopy (XPS) and scanning electron microscopy (SEM) are key analytical techniques that can characterize the changes in functional groups, crystal structure, surface element composition, and morphology of adsorbents before and after adsorption, thus verifying the actual existence of the proposed adsorption mechanisms and providing experimental support for the in-depth interpretation of adsorption micro-mechanisms.

5.2.1. Computational Chemistry Studies

The aim of computational chemistry, a branch of theoretical chemistry, is to understand chemical problems by utilizing efficient mathematical approximations and computer programs to calculate molecular properties and simulate chemical behaviors. Computational chemistry studies of adsorbents and adsorption processes typically employ quantum chemical and MD methods.

Quantum chemistry employs the Schrödinger equation to directly address electronic structure issues, making it particularly suitable for analyzing electron-level interactions in adsorption processes. Density functional theory (DFT) is a powerful quantum chemical tool that can bridge experimental observations and theoretical predictions across a wide range of molecular properties. DFT calculations determine the most stable adsorption configurations (e.g., top, bridge, or hollow sites) and their energies on surfaces, revealing the nature of active sites (e.g., hybridization between metal d-orbitals and adsorbate orbitals). Bader charge analysis or Mulliken population analysis quantifies the charge redistribution between adsorbates and substrates. Zhou et al. [145] demonstrated that cancrinite is the key component influencing phosphate adsorption in red mud. Using DFT, researchers optimized the cancrinite structure, the primary component of red mud, and modified it with sodium dodecylbenzenesulfonate. Abadee et al. [146] investigated the interactions between phenol and water molecules with graphene and graphene nanobuds (GNB) using the DFT-D3 method and revPBE/def2-TZVP theoretical model. Compared to phenol, water molecules exhibited weaker interactions with graphene and GNB. GNB demonstrated stronger adsorption affinity for phenol than water molecules at the fullerene cage top, near the neck region, and on the graphene surface. This phenomenon can be attributed to the concurrent π–π stacking and electrostatic attraction in the phenol/adsorbent system. DFT-D3 calculations revealed that phenol's binding energy on the graphene surface is approximately 11 kcal·mol^{-1} higher than that of water molecules, which stems from the strong π–π interactions between phenol and the graphene surface proximity. In contrast, water molecules only engage in electrostatic interactions. Zhou et al. [147] investigated the adsorption mechanisms between functionalized carbon surfaces and VOCs using quantum chemical calculations. The O/N functional groups and MgO nanoparticles significantly enhanced the adsorption of the acetone monolayer under low relative pressure through hydrogen bonding and electrostatic interactions.

MD calculations, which simulate nuclear motion using classical force fields, are well-suited for studying dynamic processes and temperature/pressure effects. They can model real-time molecular interactions, such as diffusion, collisions, and surface adsorption (e.g., methane migration in MOF channels), and reveal how entropy effects influence adsorption. Through MD simulations, Wei et al. [148] confirmed that the adsorption of four chlorophenolic environmental hormones (EHs) on the surface of graphene oxide (GO) exhibited a three-phase motion pattern. The MD simulations also verified that the GO–OH system demonstrated superior adsorption affinity for EHs compared to the GO–O system, and an increase in oxidation degree (number of oxygen-containing functional groups) enhanced adsorption stability. According to the calculations, the complexes of GOs and 2,4-dichlorophenol (DCP) were optimized, as shown in Figure 7A. Compared with the (GO–O–) system, the hydrogen bond distance between (GO–OH) and DCP is significantly closer, indicating enhanced hydrogen bonding interactions. Simulations of complexes with different EH molecules also demonstrated similar trends. To validate the enhanced wettability and adsorption performance of modified cancrinite in red mud, Zhou et al. [145] investigated the kinetic relaxation characteristics of phosphate-containing water clusters on cancrinite (unmodified) and sodium dodecylbenzenesulfonate (SDBS)-wetted modified cancrinite surfaces (Figure 7B). The reaction processes of the three phosphate-containing water clusters on both cancrinite surfaces exhibited similarities: initially, water clusters adhered to the cancrinite surface. After relaxation, oxygen atoms from water molecules and phosphate ions migrated toward the surface, completing adsorption. This resulted in the rupture of the wettability film on the phosphate-containing water clusters and a reduction in hydrogen bond numbers within the clusters, enabling phosphate adsorption on the cancrinite surface. Following relaxation, phosphate-containing water clusters on the modified cancrinite surface achieved complete spreading and adsorption, whereas water clusters on the unmodified cancrinite surface formed new small clusters for adsorption, demonstrating significantly weaker spreading effects compared to the modified group.

5.2.2. Analytical Instrument Measurements

Analytical instrumentation techniques, FTIR, XRD, XPS, and SEM, play a crucial role in investigating the mechanisms of adsorption processes. The combined use of these analytical techniques, along with adsorption kinetics, isotherms, and thermodynamic analysis, enables a comprehensive understanding of the adsorption process mechanisms [149].

(1) FTIR

FTIR spectroscopy can detect changes in the peak positions of functional groups on the adsorbent before and after adsorption, thereby identifying the active sites involved in adsorption. Feng et al. [114] investigated the changes in infrared spectra of the adsorbent LC@SRBC before and after the adsorption of PSNPs from water. After adsorption, LC@SRBC showed distinct peaks characteristic of PSNPs, directly confirming their successful adsorption and immobilization. The intensity of the –OH stretching vibration peak at 3438 cm^{-1} was significantly reduced post-adsorption, indicating that the hydroxyl groups from lignin and chitosan participated in the adsorption process, with the attenuation of this peak intensity correlating with the amount of PSNPs adsorbed. The oxygen-containing functional groups on the surface of LC@SRBC, such as hydroxyl (–OH) and C–O–C, formed hydrogen bonds with the corresponding functional groups on the surface of PSNPs. The reduced intensity of the –OH peak in the FTIR spectrum post-adsorption indicated that these oxygen-containing functional groups enhanced the adsorbent's affinity for PSNPs through hydrogen bonding, serving as one of the key driving forces in the adsorption process. PSNPs contain benzene ring structures, while the aromatic structures on the surface of LC@SRBC (derived from the carbon skeletons of sludge and lignin) can form π–π

interactions with the benzene rings of PSNPs. Zhong et al. [6] investigated the functional group changes in red mud before and after modification and Ni^{2+} adsorption through FTIR analysis. After modification, the characteristic peaks of Al–O–Al and Si–O–Si disappeared, indicating that some aluminosilicates dissolved under strong alkaline hydrothermal conditions. The peak shapes near 995 cm^{-1} and 463 cm^{-1} changed, corresponding to the transformation from non-zoisite-type aluminosilicate frameworks to zeolite-type frameworks (adjustment of T–O–T and T–O vibration modes), confirming that the hydrothermal modification successfully converted some aluminosilicates into zeolite structures. The T–O bending vibration peak originally near 463 cm^{-1} shifted to 473 cm^{-1}, indicating a change in the cation type within the zeolite framework (Ni^{2+} replaced Na^{+} and Ca^{2+}) and indirectly confirming the existence of the cation exchange mechanism. The FTIR feature and the possible adsorption mechanisms of Ni^{2+} by MRM are shown in Figure 8A,B.

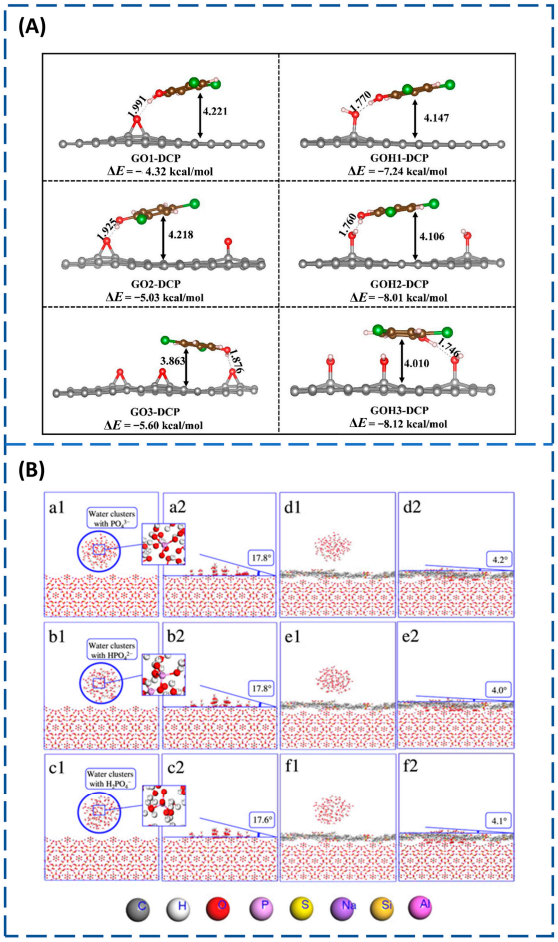


Figure 7. (**A**) The optimized geometries of 2,4-dichlorophenol (DCP) adsorbed onto G(O)s and G(OH)s with different oxygen-containing functional groups (calculated via DFT-PBE). Reprinted with permission from reference [148]. Copyright 2019, Elsevier. (**B**) Dynamics relaxation of phosphate-containing water clusters on the surface of cancrinite (space group P63/m) and wetting-modified cancrinite: a1, a2, d1, and d2 are water clusters with PO_4^{3-}; b1, b2, e1, and e2 are water clusters with HPO_4^{2-}; c1, c2, f1, and f2 are water clusters with $H_2PO_4^{-}$ [145]. Copyright 2022, IOP Publishing.

(2) XRD

XRD analysis can reveal changes in the lattice structure before and after adsorption, providing crucial insights for studying adsorbents with well-defined crystalline structures or adsorption processes that result in crystal formation. The XRD spectra of MRM prepared by Zhong et al. [6] before Ni^{2+} adsorption exhibited characteristic peaks corresponding

to $Ca(OH)_2$, hematite, and zeolite. After adsorption, the $Ca(OH)_2$ diffraction peak almost disappeared, indicating its removal during adsorption. Additionally, a significant shift in the zeolite characteristic peak was detected post-adsorption, which may be attributed to the partial substitution of cations in the zeolite framework. The XRD spectra are shown in Figure 8A. Chen et al. [91] also used XRD to investigate the adsorption mechanism of methylene blue by NaP1 zeolite. When comparing XRD spectra of methylene blue adsorbed onto red mud-derived zeolites, the characteristic peak intensity of NaP1 zeolite decreased after adsorption. Still, the peak position remained unchanged without new methylene blue-related diffraction peaks appearing. This fact indicates that methylene blue molecules did not disrupt the crystalline framework of NaP1 zeolite, demonstrating surface/channel-filling-type adsorption. It can also be inferred that methylene blue molecules are primarily loaded in amorphous states within zeolite channels or on their surfaces, without entering the crystalline lattice to induce phase transformation. The crystallinity of zeolites positively correlates with adsorption capacity, where high crystallinity implies a more developed pore network that enables efficient methylene blue capture through steric hindrance effects and van der Waals forces.

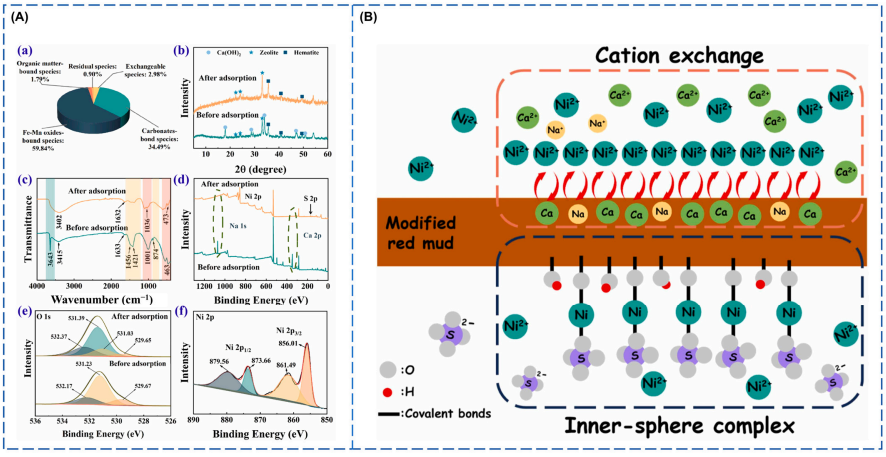


Figure 8. (**A**) Characterization of MRM: (**a**) Distribution of the adsorbed Ni^{2+} fractions; (**b**) XRD patterns, (**c**) FTIR spectra, and (**d**–**f**) XPS spectra before and after Ni^{2+} adsorption. (**B**) Possible adsorption mechanisms of Ni^{2+} by MRM. Reprinted with permission from reference [6]. Copyright 2024, Elsevier.

(3) XPS

XPS serves as a powerful surface analysis technique for determining the elemental composition and chemical states of adsorbents. In the Ni^{2+} adsorption experiment conducted by Zhong et al. [6], the post-adsorption XPS full-scan spectrum revealed characteristic peaks associated with Ni 2p and S 2p, indicating successful adsorption of Ni^{2+} and trace SO_4^{2-} onto MRM. Notably, peaks corresponding to Na 1s and Ca 2p completely disappeared after adsorption, confirming cation exchange during the process. The peak areas of NaO, FeO, CaOH, and FeOH were significantly reduced post-adsorption, suggesting replacement of Na^+ and Ca^{2+} in MRM by Ni^{2+}. High-resolution Ni 2p spectroscopy revealed two distinct Ni 2p peaks at 873.66 eV and 856.01 eV in the adsorbed MRM. The XPS image is shown in Figure 8A. In the methylene blue adsorption experiments conducted by Chen et al. [91], the XPS full spectrum of NaP1 zeolite exhibited only Si 2p, Al 2p, O 1s, and Na 1s characteristic peaks before methylene blue adsorption. After methylene blue adsorption, a new N 1s characteristic peak appeared in the spectrum, indicating the nitrogen-containing heterocyclic structure of methylene blue molecules. The binding energies of Si 2p (approximately 102.5 eV) and Al 2p (approximately 74.5 eV) showed no significant shifts post-adsorption, suggesting that the Si–O–Si and Si–O–Al bond structures within the zeolite framework

remained stable and were not involved in chemical adsorption reactions. Before adsorption, the O 1s spectrum could be divided into two peaks corresponding to the framework oxygen (Si–O/Al–O, approximately 530.0 eV) and surface –OH (approximately 531.5 eV). Following methylene blue adsorption, the intensity of the surface hydroxyl oxygen peak decreased significantly, indicating hydrogen bonding interactions between the surface –OH groups and methylene blue molecules. The hydroxyl groups functioned as hydrogen bond donors, forming hydrogen bonds with nitrogen atoms in methylene blue molecules, thereby enhancing the adsorption affinity. Post-adsorption, the N 1s spectrum could be fitted into two peaks corresponding to the protonated amino groups ($–NH_3^+$, approximately 402.0 eV) and aromatic ring nitrogen (approximately 399.5 eV) in methylene blue molecules. Given the negative surface charge of NaP1 zeolite (resulting from Al^{3+} substituting Si^{4+} in the framework), electrostatic attraction is hypothesized to be a key adsorption mechanism: the negatively charged zeolite surface interacts with the positively charged methylene blue cation ($–NH_3^+$) through electrostatic force.

(4) SEM

SEM analysis typically reveals morphological changes in adsorbents before and after adsorption, enabling assessment of structural stability during the process. Li et al. [12] conducted SEM tests on zeolites before and after Ni^{2+} adsorption. As shown in Figure 9, the cubic structure of the zeolites remained largely intact post-adsorption, with well-defined edges. EDS analysis revealed that the sodium atomic percentage in the zeolites decreased from 14.5% to 8.1% after Ni^{2+} adsorption, while RML-NaA zeolites adsorbed 3.6% of nickel. The calculated $\Delta n(Ni^{2+}):\Delta n(Na^+)$ ratio was 1:1.78, deviating from the theoretical 1:2 ratio under the ion-exchange mechanism. The results observed suggest that electrostatic interactions and surface complexations, in addition to ion exchanges, play significant roles in the adsorption process. The structural stability observed via SEM provides a structural basis for these mechanisms. The scanning electron microscopy–energy-dispersive X-ray spectroscopy (SEM-EDS) analysis result and the proposed adsorption mechanisms are illustrated in Figure 9.

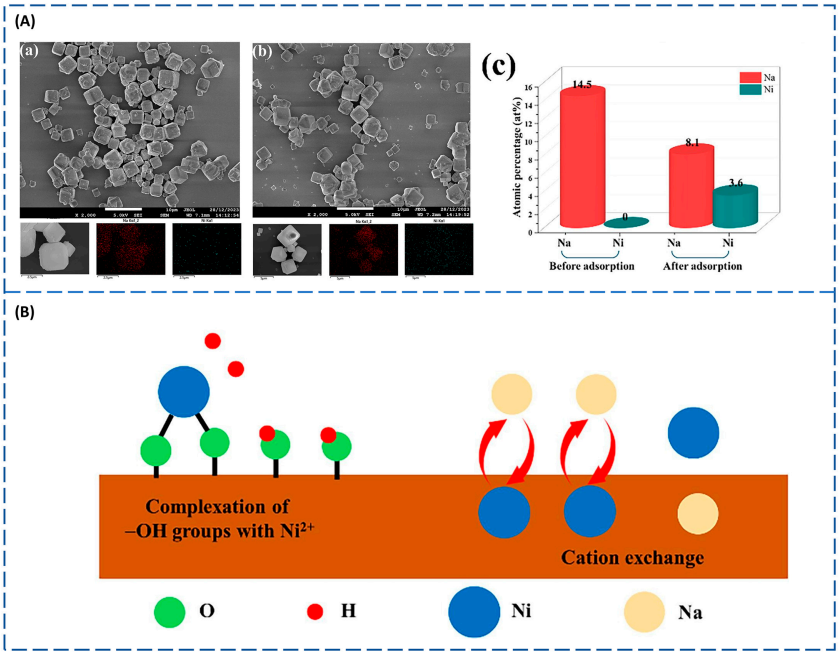


Figure 9. (**A**) SEM spectrum and mapping scanning images of RML—NaA zeolite (**a**) before and (**b**) after Ni^{2+} adsorption; (**c**) EDS analysis of RML—NaA zeolite after Ni^{2+} adsorption. (**B**) Schematic diagram of the interaction mechanisms between RML—NaA zeolite and Ni^{2+}. Reprinted with permission from reference [12]. Copyright 2025, Elsevier.

6. Conclusions and Prospects

This review comprehensively summarizes the research progress, application practices, and adsorption mechanisms of adsorbents derived from IISWs, systematically organizing the core findings from the cited literature, clarifying optimal technical routes, and outlining future development directions for this field. This approach provides a clear reference for resource utilization in IISWs and for the development of low-cost, high-efficiency adsorbents.

6.1. Conclusions

The core findings of this review can be summarized as follows.

(1) IISWs, including red mud, zinc slag, lithium slag, EMR, phosphogypsum, WTS, sewage sludge, BFS, steel slag, CFA, CGS, CSS, and LSS, are residues treated via chemically dominated processes. They are characterized by complex compositions and challenges in utilization. Among the various IISWs involved in this review, CFA and BFS show excellent adsorption potential in nature. Due to their inherent porous structure, stable chemical properties, and abundant active components (e.g., Si and Al), CFA and BFS can be converted into high-performance adsorbents with simple modification treatments, and their adsorption capacity and cycling stability are significantly superior to other IISWs. In contrast, red mud, EMR, and phosphogypsum have relatively poor adsorption properties due to their high toxicity and complex composition, requiring more stringent modification treatments to achieve effective adsorption performance. Converting IISWs into adsorbents helps reduce these solid wastes, offering significant environmental benefits.

(2) In terms of the suitable procedures and treatments for adsorbent synthesis, physical modification (e.g., thermal activation and ball milling) and chemical modification (e.g., acid-base activation and metal oxide loading) are the most widely used and effective synthesis procedures for IISWs-derived adsorbents. In general, chemical modification methods are more effective than physical modification methods in improving the adsorption efficiency of IISWs-derived adsorbents. Among chemical modification methods, acid activation (using sulfuric acid, hydrochloric acid, etc.) can effectively remove impurities on the surface of IISWs, increase the specific surface area and pore volume, and expose more active sites; metal oxide loading (Fe_3O_4, TiO_2, ZnO, etc.) can introduce new active components, enhance the electrostatic interaction and complexation ability between adsorbents and analytes; and surfactant modification (e.g., cetyltrimethylammonium bromide) can change the surface charge properties of adsorbents, improving their selectivity for specific analytes. Among these, the combined modification of acid activation and Fe_3O_4 loading has the most significant effect on improving adsorption efficiency, which can increase the adsorption capacity of IISWs-derived adsorbents by 2–5 times compared with unmodified ones, and also improve the separation performance of adsorbents due to the magnetic properties of Fe_3O_4. Compared with single modification methods, combined modification procedures can synergistically optimize the physical and chemical properties of adsorbents, making them more suitable for practical adsorption scenarios.

(3) For the analytes suitable for adsorption by IISWs-derived adsorbents, the existing literature shows that such adsorbents have broad applicability, but they exhibit obvious selectivity for different analytes. Specifically, they are most suitable for the adsorption of heavy metal ions (e.g., Pb^{2+}, Cd^{2+}, Cr^{6+}, and Cu^{2+}) in aqueous solutions, which is mainly attributed to the strong electrostatic interaction and ion exchange effect between the active sites (e.g., hydroxyl groups and carboxyl groups) on the surface of the adsorbents and heavy metal ions. In addition, IISWs-derived adsorbents also have good adsorption effects on anionic pollutants (e.g., phosphate, nitrate, and fluoride)

and organic pollutants (e.g., dyes and phenols). Still, their adsorption capacity for organic pollutants is generally lower than that for heavy metal ions. Among them, modified CFA and BFS adsorbents have the best adsorption effect on Pb^{2+} and Cr^{6+}, with adsorption capacities often exceeding 100 $mg \cdot g^{-1}$ after reasonable modification. During the adsorption processes, multiple adsorption mechanisms often coexist, such as van der Waals forces, electrostatic interactions, π–π interactions, ion exchanges, and complexations. Due to differences in the types and properties of adsorbents, particularly in the case of composite adsorbents, the adsorption mechanisms become more complex.

6.2. Prospects

Despite the significant progress made in the preparation and application of IISWs-derived adsorbents, there are still some problems to be solved in this field, and the future development directions can be clarified as follows.

(1) Further optimize the synthesis process of adsorbents, develop low-cost, environmentally friendly modification methods, reduce the energy consumption and environmental impact of the preparation process, and realize the large-scale industrial production of IISWs-derived adsorbents.
(2) Conduct in-depth research on the adsorption mechanisms of IISWs-derived adsorbents, especially the synergistic effect of multiple adsorption mechanisms in the adsorption process, to provide a theoretical basis for the design and modification of high-performance adsorbents.
(3) Strengthen the research on the long-term stability and cycling performance of adsorbents, develop effective desorption and regeneration technologies, extend the service life of adsorbents, and reduce the cost of practical application.
(4) Expand the application scope of IISWs-derived adsorbents, explore their application in the adsorption of emerging pollutants (e.g., microplastics and antibiotics), and develop composite adsorbents with multi-functional adsorption performance.
(5) Establish a comprehensive evaluation system for IISWs-derived adsorbents, considering their adsorption performance, preparation cost, environmental impact, and practical applicability, to promote the industrial application and sustainable development of this technology.
(6) Due to the complex composition and structures of both IISWs and IISWs-derived adsorbents, future efforts can leverage artificial intelligence (AI) technologies and quantitative structure-activity relationship (QSAR) models to establish correlations linking structures of IISWs and IISWs-derived adsorbents, adsorption conditions, adsorption performance of adsorbents, and environmental impacts. This approach will drive the transition of IISWs-derived adsorbents toward data-driven design.

In summary, the preparation of adsorbents from IISWs not only realizes the resource utilization of solid wastes, solves the problems of large volume and difficult treatment of IISWs, but also provides a low-cost alternative for the preparation of adsorbents, which has important economic, environmental, and social significance. With the in-depth research on modification technologies and adsorption mechanisms, IISWs-derived adsorbents are expected to play a more important role in environmental pollution control in the future.

Supplementary Materials: The following supporting information can be downloaded at: https://www.mdpi.com/article/10.3390/separations13030083/s1, Table S1: Adsorption properties of industrial inorganic solid wastes (IISWs)-derived adsorbents, Table S2: Comparison of application fields and characteristics for IISWs-derived Adsorbents.

Author Contributions: Conceptualization, S.W.; methodology, R.D.; validation, R.D. and X.L.; formal analysis, R.D.; investigation, R.D.; resources, S.W.; writing—original draft preparation, R.D.; writing—review and editing, R.D., X.L. and S.W.; visualization, R.D.; supervision, S.W.; project administration, S.W. All authors have read and agreed to the published version of the manuscript.

Funding: This research was funded by the National Key Research and Development Program of China, grant number 2023YFC2908203; the Major Project of Science and Technology of Guizhou Province, China, grant number [2024]017; and the College Student Innovation and Entrepreneurship Project of Hunan Province, China, grant number S2021105330916.

Data Availability Statement: No new data were created or analyzed in this study.

Conflicts of Interest: The authors declare no conflicts of interest.

Abbreviations

The following abbreviations are used in this manuscript:

4Rs	Four-membered rings
ADP	Ammonium dihydrogen phosphate
AEMR	Activated electrolytic manganese residue
AI	Artificial Intelligence
Al-WTR	Aluminum-based water treatment residue
APTES	3-Aminopropyltriethoxysilane
APTMS	3-Aminopropyltrimethoxysilane
ARM	Activated red mud
ARM/NiOOH	Activated red mud immobilized flake-shaped NiOOH
BASs	Bronsted acid sites
BFS	Blast furnace slag
BFSZ	BFS-based zeolite
BRM	Burning raw material
C_0	Initial concentration
CCBM	Coal-based cemented backfill material
CCR	Calcium carbide residue
CFA	Coal fly ash
CFBFA	Circulating fluidized bed fly ash
CGCS	Coal gasification coarse slag
CGS	Coal gasification slag
CGF	Composite granular filler
CMC-SSBC-3	Sewage sludge biochar modified with carboxymethyl chitosan
COS	Carbonyl sulfide
CPB	Cement paste backfilling
CS	Carbide slag
CSD	Copper smelting dust
CSS	Copper smelting slag
CS-AAMs	Copper slag-based alkali-activated microspheres
D6R	Double six-membered ring
DCP	2,4-Dichlorophenol
DFT	Density functional theory
DG	Desulfurized gypsum
DGMC600	Distillers' grains-modified engineered biochar
DWTS	Drinking water treatment sludge
EB	EMR-biochar
EDS	Energy-dispersive X-ray spectroscopy
EGC	Engineered geopolymer composites
EH	Environmental hormone
EMR	Electrolytic manganese residue

EMRC	EMR flotation concentrate
EMRZ	EMR-derived zeolite
EMRZA	EMR-derived zeolite A
EMRZX	EMR-derived zeolite X
ERZ	Zeolite X synthesized with EMR and red mud as the main raw materials
ESP	Exchangeable sodium percentage
FA	Fly ash
FAU	A type of zeolite, including zeolite X and zeolite Y
Fe-WTR	Iron-modified/Iron-based water treatment residue
FTIR	Fourier transform infrared spectroscopy
GGBS	Ground granulated blast-furnace slag
GHG	Greenhouse gas
GNB	Graphene nanobuds
GO	Graphene oxide
GRM	Granular red mud
HCPC	High-content phosphogypsum cementitious
HPMC	Hydroxypropyl methylcellulose
IISWs	Industrial inorganic solid wastes
IPC	Iron phosphate cement
LASs	Lewis acid sites
LC@SRBC	Lignin-modified spontaneous magnetic sludge-based biochar
LF	Ladle furnace
LFS	Ladle furnace slag
LLR	Lithium leaching residue
LS	Lithium slag
LSS	Lead smelting slag
LZSS	Lead-zinc smelting slag
MB	Methylene blue
MD	Molecular dynamics
MgAl-LDO	Magnesium-aluminum layered double oxide
MRM	Modified red mud
MRM-PS	Modified red mud with polystyrene
NO_x	Nitrogen oxides
OFL	Ofloxacin
PFAS	Perfluoro and polyfluoroalkyl substances
PFOA	Perfluorooctanoic acid
PFOS	Perfluorooctane sulfonic acid
PMBC	Phosphogypsum-modified biochar composite
PMMA	Polymethyl methacrylate
PS	Polystyrene
PSNPs	Polystyrene nanoplastics
PTFE	Polytetrafluoroethylene
q_e	Equilibrium adsorption capacity
q_m	Maximum adsorption capacity
QSAR	Quantitative structure-activity relationship
RAS	A kind of low-carbon curing agent synthesized using red mud, GGBS, CCR, and phosphogypsum
REEs	Rare earth elements
RM	Red mud
RMMC	Red mud-based modified ceramsites
RM-PGCM	Red mud-phosphogypsum-based composite cementitious materials
SDBS	Sodium dodecylbenzenesulfonate
SEM	Scanning electron microscopy
SEM-EDS	Scanning electron microscopy–energy-dispersive X-ray spectroscopy
SH-CGCS	Sodium hydroxide-activated CGCS

SLR	Spodumene leaching residue
SMX	Sulfamethoxazole
SNR	Sea nodule residue
SS	Steel slag
SSNMR	Solid-state nuclear magnetic resonance
TG	Thermogravimetric analysis
TMP	Trimethoprim
TYBC	TiO_2-loaded phosphogypsum-modified biochar
VOCs	Volatile organic compounds
WTS	Water treatment sludge
WTR	Water treatment residue
XPS	X-ray photoelectron spectroscopy
XRD	X-ray diffraction
XRF	X-ray fluorescence spectrometry
YPS	Yellow phosphorus slag
ZAS	Zinc-aluminum silicate
ZAS/GRM	Zinc-aluminum silicate modified granular red mud
ZLR	Zinc leaching residue
ZVI	Zero-valent iron
ΔG	Change in Gibbs free energy
ΔH	Change in enthalpy
ΔS	Change in entropy

References

1. Xiong, Y.X.; He, M.; Wu, Y.T.; Su, Y.N.; Li, M.; Yin, M.C.; Zhang, A.T.L.; Li, X.; Li, S.; Yang, Y.; et al. A comprehensive review on the utilization of industrial solid waste in thermal energy storage field. *Sol. Energy Mater. Sol. Cells* **2025**, *285*, 113562. [CrossRef]
2. Della Rocca, D.G.; Peralta, R.M.; Peralta, R.A.; Rodríguez-Castellón, E.; Moreira, R. Adding value to aluminosilicate solid wastes to produce adsorbents, catalysts and filtration membranes for water and wastewater treatment. *J. Mater. Sci.* **2021**, *56*, 1039–1063. [CrossRef]
3. Crini, G.; Lichtfouse, E.; Wilson, L.D.; Morin Crini, N. Conventional and non-conventional adsorbents for wastewater treatment. *Environ. Chem. Lett.* **2019**, *17*, 195–213. [CrossRef]
4. Cao, X.Y.; Wang, Q.; Wang, S.; Man, R.L. A novel polystyrene-poly(hydroxamic acid) interpenetrating polymer network and its adsorption towards rare earth ions. *J. Rare Earths* **2022**, *40*, 127–134. [CrossRef]
5. Yu, T.; Chen, Z.; Liu, Z.D.; Xu, J.H.; Wang, Y.D. Review of hydrogen sulfide removal from various industrial gases by zeolites. *Separations* **2022**, *9*, 229. [CrossRef]
6. Zhong, W.; Li, X.T.; Ma, X.; Cao, Z.F.; Zhong, H.; Yang, J.; Wang, S. Transferring red mud to efficient adsorbent for the adsorption and immobilization of Ni(II) from aqueous solution. *Colloids Surf. C Environ. Asp.* **2024**, *2*, 100045. [CrossRef]
7. Ma, X.; Duan, G.Y.; Huang, J.Q.; Yang, J.; Cao, Z.F.; Wang, S. Preparation of graphene oxide/polyiminodiacetic acid resin as a high-performance adsorbent for Cu(II). *J. Cent. South Univ.* **2023**, *30*, 3881–3896. [CrossRef]
8. Li, G.Q.; Du, R.L.; Cao, Z.F.; Li, C.X.; Xue, J.R.; Ma, X.; Wang, S. Research progress in graphene-based adsorbents for wastewater treatment: Preparation, adsorption properties and mechanisms for inorganic and organic pollutants. *C* **2024**, *10*, 78. [CrossRef]
9. Zhang, T.; Liu, X.X.; Qu, G.F.; Lu, P.; Wang, J.; Wu, F.H.; Ren, Y.C. Secondary resource utilization of metallurgical solid waste: Current status and future prospects of wet extraction of valuable metals. *Sep. Purif. Technol.* **2025**, *361*, 131278. [CrossRef]
10. Cheje Machaca, D.M.; Botelho, A.B.; de Carvalho, T.C.; Tenório, J.A.S.; Espinosa, D.C.R. Hydrometallurgical processing of chalcopyrite: A review of leaching techniques. *Int. J. Miner. Metall. Mater.* **2024**, *31*, 2537–2555. [CrossRef]
11. Liu, X.; Han, Y.X.; He, F.Y.; Gao, P.; Yuan, S. Characteristic, hazard and iron recovery technology of red mud—A critical review. *J. Hazard. Mater.* **2021**, *420*, 126542. [CrossRef]
12. Li, X.T.; Zhong, W.; Cao, Z.F.; Zhong, H.; Xue, J.R.; Li, C.X.; Ma, X.; Wang, S. A green red mud utilization process for Fe, Al, and Si extraction and NaA–zeolite synthesis for wastewater treatment. *Appl. Surf. Sci.* **2025**, *689*, 162481. [CrossRef]
13. Song, S.L.; Sun, W.; Wang, L.; Liu, R.Q.; Han, H.S.; Hu, Y.H.; Yang, Y. Recovery of cobalt and zinc from the leaching solution of zinc smelting slag. *J. Environ. Chem. Eng.* **2019**, *7*, 102777. [CrossRef]
14. Li, C.B.; Zhang, G.F.; Zheng, H.; Zhang, F.; Liu, K. Characterization of glass-ceramics developed from zinc leaching residue by sintering method. *Ceram. Int.* **2024**, *50*, 8302–8317. [CrossRef]
15. Huang, S.Z.; Wang, Y.; Zhang, L.; Zhu, S.J.; Ma, Z.F.; Cui, Q.; Wang, H.Y. Insight into the kinetic behavior of microwave-assisted synthesis of NaX zeolite from lithium slag. *New J. Chem.* **2023**, *47*, 14335–14343. [CrossRef]

16. Li, X.Y.; Du, R.L.; Li, X.T.; Li, C.X.; Cai, H.Y.; Zhu, T.H.; Ma, X.; Wang, S. Converting electrolytic manganese residue to pure, single-phase, spherical zeolite P for high-efficiency adsorption of Mn^{2+} and NH_4^+. *Sep. Purif. Technol.* **2025**, *364*, 132369. [CrossRef]
17. Cao, W.X.; Yi, W.; Peng, J.H.; Li, J.; Yin, S.H. Recycling of phosphogypsum to prepare gypsum plaster: Effect of calcination temperature. *J. Build. Eng.* **2022**, *45*, 103511. [CrossRef]
18. Nguyen, M.D.; Thomas, M.; Surapaneni, A.; Moon, E.M.; Milne, N.A. Beneficial reuse of water treatment sludge in the context of circular economy. *Environ. Technol. Innov.* **2022**, *28*, 102651. [CrossRef]
19. Li, C.X.; Li, X.; Yu, Y.; Zhang, Q.W.; Li, L.; Zhong, H.; Wang, S. A novel conversion for blast furnace slag (BFS) to the synthesis of hydroxyapatite-zeolite material and its evaluation of adsorption properties. *J. Ind. Eng. Chem.* **2022**, *105*, 63–73. [CrossRef]
20. Li, Y.R.; Liao, H.Q.; Guo, Y.X. Aqueous carbonation of steel slag and preparation of calcium carbon: A new strategy for the utilization of steel slag. *J. Environ. Chem. Eng.* **2025**, *13*, 115951. [CrossRef]
21. Liu, W.H.; Li, H.; Zhu, H.M.; Xu, P.J. Properties of a steel slag–permeable asphalt mixture and the reaction of the steel slag–asphalt interface. *Materials* **2019**, *12*, 3603. [CrossRef] [PubMed]
22. Feng, W.; Wan, Z.J.; Daniels, J.; Li, Z.K.; Xiao, G.K.; Yu, J.L.; Xu, D.; Guo, H.; Zhang, D.K.; May, E.F.; et al. Synthesis of high quality zeolites from coal fly ash: Mobility of hazardous elements and environmental applications. *J. Clean. Prod.* **2018**, *202*, 390–400. [CrossRef]
23. Guo, Q.; Tan, L.Y.; Li, M.; Yin, Z.J.; Sun, Z.H.; Xia, Y.Y. Preparation and performance of alkali-activated coal gasification slag-based backfill materials. *Appl. Sci.* **2025**, *15*, 8995. [CrossRef]
24. Luo, Y.L.; Zhou, X.T.; Luo, Z.Q.; Ma, H.Y.; Wei, Y.; Liu, Q. A novel iron phosphate cement derived from copper smelting slag and its early age hydration mechanism. *Cem. Concr. Comp.* **2022**, *133*, 104653. [CrossRef]
25. Han, J.W.; Liu, W.; Qin, W.Q.; Zhang, T.F.; Chang, Z.Y.; Xue, K. Effects of sodium salts on the sulfidation of lead smelting slag. *Miner. Eng.* **2017**, *108*, 1–11. [CrossRef]
26. Zhao, Z.Z.; Liu, W.H.; Jiang, Y.W.; Wan, Y.F.; Du, R.H.; Li, H. Solidification of heavy metals in lead smelting slag and development of cementitious materials. *J. Clean. Prod.* **2022**, *359*, 132134. [CrossRef]
27. Liang, Q.; Zhang, M.H.; Liang, C.; Chen, H.C. Modified red mud tailored to chromium contaminated soil remediation. *J. Environ. Chem. Eng.* **2023**, *11*, 109720. [CrossRef]
28. Zhou, P.X.; Qi, J.M.; Yang, D.; Li, B.; Zhou, Y. Purification of low-concentration carbonyl sulfide by red mud-based adsorbent. *Bull. Environ. Contam. Toxicol.* **2022**, *109*, 194–201. [CrossRef]
29. He, Z.H.; Du, S.G.; Chen, D. Microstructure of ultra high performance concrete containing lithium slag. *J. Hazard. Mater.* **2018**, *353*, 35–43. [CrossRef]
30. Han, G.F.; Gu, D.L.; Lin, G.; Cui, Q.; Wang, H.Y. Recovery of lithium from a synthetic solution using spodumene leach residue. *Hydrometallurgy* **2018**, *177*, 109–115. [CrossRef]
31. Li, C.X.; Zhong, H.; Wang, S.; Xue, J.R.; Zhang, Z.Y. Removal of basic dye (methylene blue) from aqueous solution using zeolite synthesized from electrolytic manganese residue. *J. Ind. Eng. Chem.* **2015**, *23*, 344–352. [CrossRef]
32. Li, W.L.; Jin, H.X.; Xie, H.Y.; Ma, L.R. Synthesis of zeolite A and zeolite X from electrolytic manganese residue, its characterization and performance for the removal of Cd^{2+} from wastewater. *Chin. J. Chem. Eng.* **2023**, *62*, 31–45. [CrossRef]
33. Li, W.L.; Jin, H.X.; Xie, H.Y.; Wang, M.L.; Wang, X. Electrolytic manganese residue and red mud co-treatment: Synthesizing zeolite X and adsorbing leaching solution from electrolytic manganese residue. *Sep. Purif. Technol.* **2025**, *356*, 129795. [CrossRef]
34. Levickaya, K.; Alfimova, N.; Nikulin, I.; Kozhukhova, N.; Buryanov, A. The use of phosphogypsum as a source of raw materials for gypsum-based materials. *Resources* **2024**, *13*, 69. [CrossRef]
35. Zeng, C.X.; Guan, Q.J.; Sui, Y.; Yu, W.J.; Bu, Y.J.; Liu, C.F.; Zhang, Z.Y. Kinetics of nitric acid leaching of low-grade rare earth elements from phosphogypsum. *J. Cent. South Univ.* **2022**, *29*, 1869–1880. [CrossRef]
36. Ling, Y.P.; Tham, R.H.; Lim, S.M.; Fahim, M.; Ooi, C.H.; Krishnan, P.; Matsumoto, A.; Yeoh, F.Y. Evaluation and reutilization of water sludge from fresh water processing plant as a green clay substituent. *Appl. Clay Sci.* **2017**, *143*, 300–306. [CrossRef]
37. Balkaya, M. Evaluation of the geotechnical properties of alum sludge, zeolite, and their mixtures for beneficial usage. *Environ. Prog. Sustain. Energy* **2015**, *34*, 1028–1037. [CrossRef]
38. El-Didamony, H.; Khalil, K.A.; Heikal, M. Physico-chemical and surface characteristics of some granulated slag–fired drinking water sludge composite cement pastes. *HBRC J.* **2014**, *10*, 73–81. [CrossRef]
39. Li, C.X.; Li, X.; Zhang, Q.W.; Li, L.; Wang, S. The alkaline fusion-hydrothermal synthesis of blast furnace slag-based zeolite (BFSZ): Effect of crystallization time. *Minerals* **2021**, *11*, 1314. [CrossRef]
40. Chouchane, T.; Chibani, S.; Khiriddine, O.; Boukari, A. Adsorption study of Pb(II) ions on the blast furnace slag (BFS) from aqueous solution. *Iran. J. Mater. Sci. Eng.* **2023**, *20*, 1–13.
41. Zhan, X.H.; Xiao, L.P.; Liang, B. Removal of Pb(II) from acid mine drainage with bentonite-steel slag composite particles. *Sustainability* **2019**, *11*, 4476. [CrossRef]

42. Liu, G.Q.; Lin, Y.X.; Zhang, L.L.; Zhang, M.W.; Gu, C.C.; Li, J.; Zheng, T.C.; Chai, J. Preparation of NaA zeolite molecular sieve based on solid waste fly ash by high-speed dispersion homogenization-assisted alkali fusion-hydrothermal method and its performance of ammonia-nitrogen adsorption. *J. Sci. Adv. Mater. Dev.* **2024**, *9*, 100673. [CrossRef]
43. Ma, W.Q.; Yi, Y.R.; Fang, M.H.; Lin, Y.; Li, C.H.; Li, J.; Liu, W. Zeolite prepared from high-calcium ladle furnace slag and fly ash for Pb^{2+} removal. *J. Water Process Eng.* **2024**, *61*, 105351. [CrossRef]
44. Zhang, J.Y.; Zuo, J.; Jiang, Y.S.; Zhu, D.D.; Zhang, J.P.; Wei, C.D. Kinetic analysis on the mesoporous formation of coal gasification slag by acid leaching and its thermal stability. *Solid State Sci.* **2020**, *100*, 106084. [CrossRef]
45. Miao, Z.K.; Guo, F.H.; Zhao, X.; Guo, Z.K.; Guo, Y.; Zhang, Y.X.; Wu, J.J. Effects of acid treatment on physicochemical properties and gasification reactivity of fine slag from Texaco gasifier. *Chem. Eng. Res. Des.* **2021**, *169*, 1–8. [CrossRef]
46. Gao, J.T.; Huang, Z.L.; Wang, Z.W.; Guo, Z.C. Recovery of crown zinc and metallic copper from copper smelter dust by evaporation, condensation and super-gravity separation. *Sep. Purif. Technol.* **2020**, *231*, 115925. [CrossRef]
47. Cao, J.L.; Wang, Y.; Yan, Z.L.; Li, G.J. Polystyrene microspheres-templated preparation of hierarchical porous modified red mud with high rhodamine B dye adsorption performance. *Micro Nano Lett.* **2014**, *9*, 229–231. [CrossRef]
48. Xu, D.M.; Fu, R.B.; Tong, Y.H.; Shen, D.L.; Guo, X.P. The potential environmental risk implications of heavy metals based on their geochemical and mineralogical characteristics in the size-segregated zinc smelting slags. *J. Clean. Prod.* **2021**, *315*, 128199. [CrossRef]
49. Benis, K.Z. Transforming drinking water treatment residuals into efficient adsorbents: A review of activation and modification methods. *Environ. Res.* **2024**, *262*, 119893. [CrossRef]
50. Gao, W.H.; Zhou, W.T.; Lyu, X.J.; Liu, X.; Su, H.L.; Li, C.M.; Wang, H. Comprehensive utilization of steel slag: A review. *Powder Technol.* **2023**, *422*, 118449. [CrossRef]
51. Yu, W.J.; Li, X.Y.; Xu, W.T.; Guan, Q.J.; Zhou, F.J.; Zhang, J.N.; Wang, L.; Wang, Y.X.; Tang, H.H. Advances in electrolytic manganese residue: Harmless treatment and comprehensive utilization. *Separations* **2025**, *12*, 180. [CrossRef]
52. Yao, Y.N.; El Naggar, M.H.; Zhang, J.X.; Xu, J.F.; Yang, J.W.; Li, M. Dynamic mechanical properties of coal-based solid waste cemented backfill material. *J. Build. Eng.* **2024**, *98*, 111347. [CrossRef]
53. Yin, X.; Ma, L.P.; Li, K.; Du, W.; Hou, P.X.; Dai, Q.X.; Xiong, X.; Xie, L.G. Preparation of phosphogypsum-based cemented paste backfill and its environmental impact based on multi-source industrial solid waste. *Constr. Build. Mater.* **2023**, *404*, 133314. [CrossRef]
54. Zhu, F.; Liu, X.; Jiang, J.; Chen, L.; Zhong, X.L.; Zhang, Z.Y.; Guo, L.; Xue, S.G. Maize straw-*Penicillium oxalicum* enhanced long-term aggregate stability in bauxite residue ameliorated with desulfurization gypsum. *J. Cent. South Univ.* **2025**, *32*, 2873–2893. [CrossRef]
55. Tang, Y.J.; Wan, Z.Y.; Luo, Y.F.; Chen, Y.L.; Wan, Q.S. Metagenomic insight into microbial regulation of nutrient cycling in amended bauxite residue under various planting strategies: Implications for soil formation. *Appl. Soil Ecol.* **2025**, *215*, 106469. [CrossRef]
56. Bossolani, J.W.; Crusciol, C.A.C.; Garcia, A.; Moretti, L.G.; Portugal, J.R.; Rodrigues, V.A.; da Fonseca, M.d.C.; Calonego, J.C.; Caires, E.F.; Amado, T.J.C.; et al. Long-term lime and phosphogypsum amended-soils alleviates the field drought effects on carbon and antioxidative metabolism of maize by improving soil fertility and root growth. *Front. Plant Sci.* **2021**, *12*, 650296. [CrossRef] [PubMed]
57. Liu, Y.; Yang, Z.; Zhang, L.S.; Wan, H.F.; Deng, F.; Zhao, Z.Q.; Wang, J.F. Characteristics of bacterial community structure and function in artificial soil prepared using red mud and phosphogypsum. *Microorganisms* **2024**, *12*, 1886. [CrossRef]
58. Shu, J.C.; Wu, H.P.; Liu, R.L.; Liu, Z.H.; Li, B.; Chen, M.J.; Tao, C.Y. Simultaneous stabilization/solidification of Mn^{2+} and NH_4^+-N from electrolytic manganese residue using MgO and different phosphate resource. *Ecotox. Environ. Safe.* **2018**, *148*, 220–227. [CrossRef]
59. Li, B.; Shu, J.C.; Chen, M.J.; Zeng, X.F.; Liu, R.L.; Yang, Y. A new basic burning raw material for simultaneous stabilization/solidification of PO_4^{3-}-P and F^- in phosphogypsum. *Ecotox. Environ. Safe.* **2023**, *252*, 114582.
60. Li, X.; Lu, P.F.; Zhang, Y.; Dong, R.; Meng, X.L.; Zhou, E.H. Synergistic valorization of red mud: Simultaneous production of hydrogen-rich syngas and high-purity Fe/Al via integrated chemical looping gasification and acid leaching. *Sep. Purif. Technol.* **2026**, *382*, 135827. [CrossRef]
61. Zhang, J.R.; Liu, Z.Y.; Liu, Z.H. An efficient and affordable hydrometallurgical process for co-treatment of copper smelting dust and arsenic sulfide residue. *J. Clean. Prod.* **2023**, *419*, 137955. [CrossRef]
62. Habibi, H.; Mokmeli, M.; Shakibania, S.; Pirouzan, D.; Pourkarimi, Z. Separation and recovery of titanium and scandium from the red mud. *Sep. Purif. Technol.* **2023**, *317*, 123882. [CrossRef]
63. Li, Y.C.; Min, X.B.; Ke, Y.; Chai, L.Y.; Shi, M.Q.; Tang, C.J.; Wang, Q.W.; Liang, Y.J.; Lei, J.; Liu, D.G. Utilization of red mud and Pb/Zn smelter waste for the synthesis of a red mud-based cementitious material. *J. Hazard. Mater.* **2018**, *344*, 343–349. [CrossRef] [PubMed]
64. He, D.J.; Chen, M.J.; Liu, H.; Wang, J.Q. Preparation of activated electrolytic manganese residue-slag-cement ternary blended cementitious material: Hydration characteristics and carbon reduction potential. *Constr. Build. Mater.* **2024**, *425*, 135990. [CrossRef]

65. Ouyang, G.S.; Li, Z.W.; Sun, T.; Ye, Z.Y.; Deng, Y.H.; Li, W.T. Greener phosphogypsum-based all-solid-waste cementitious binder with steel slag activation: Hydration, mechanical properties and durability. *J. Clean. Prod.* **2024**, *443*, 140996. [CrossRef]
66. Lian, J.Y.; Wu, C.Q.; Shui, Z.H.; Lyu, W. Effect of a recycled phosphogypsum modifier on the performance of high-content phosphogypsum cementing materials. *Materials* **2025**, *18*, 2807. [CrossRef]
67. Ke, G.J.; Li, Z.Y.; Jiang, H.S. Study on long-term solidification of all-solid waste cementitious materials based on circulating fluidized bed fly ash, red mud, carbide slag, and fly ash. *Constr. Build. Mater.* **2024**, *427*, 136284. [CrossRef]
68. Wang, Y.F.; Liu, P.; Kong, D.W.; Li, Y.; Fu, X.; Ren, C.D.; Chen, M.S. Investigation of the properties and microscopic mechanism of red mud-phosphogypsum-based composite cementitious materials. *J. Build. Eng.* **2025**, *101*, 111962. [CrossRef]
69. Luo, Q.; Liu, Y.T.; Dong, B.Q.; Ren, J.; He, Y.; Wu, K.; Wang, Y.S. Lithium slag-based geopolymer synthesized with hybrid solid activators. *Constr. Build. Mater.* **2023**, *365*, 130070. [CrossRef]
70. Li, J.; Liu, Y.C.; Ke, X.; Jiao, X.K.; Li, R.; Shi, C.J. Geopolymer synthesized from electrolytic manganese residue and lead-zinc smelting slag: Compressive strength and heavy metal immobilization. *Cem. Concr. Comp.* **2022**, *134*, 104806. [CrossRef]
71. Xu, L.Y.; Lao, J.C.; Qian, L.P.; Shi, D.D.; Lan, J.R.; Xie, T.Y.; Hou, D.S.; Huang, B.T. Upcycling red mud into high-strength high-ductility engineered geopolymer composites (EGC): Toward superior performance and sustainability. *Compos. Part B Eng.* **2025**, *305*, 112713. [CrossRef]
72. Li, Z.P.; Zhang, J.Y.; Lei, Z.X.; Gao, M.S.; Sun, J.B.; Tong, L.H.; Chen, S.M.; Wang, Y.F. Designing low-carbon fly ash based geopolymer with red mud and blast furnace slag wastes: Performance, microstructure and mechanism. *J. Environ. Manag.* **2024**, *354*, 120362. [CrossRef]
73. Zhao, H.; Gou, H.Y. Unfired bricks prepared with red mud and calcium sulfoaluminate cement: Properties and environmental impact. *J. Build. Eng.* **2021**, *38*, 102238. [CrossRef]
74. Zhou, J.; Sheng, Z.M.; Li, T.T.; Shu, Z.; Chen, Y.; Wang, Y.X. Preparation of hardened tiles from waste phosphogypsum by a new intermittent pressing hydration. *Ceram. Int.* **2016**, *42*, 7237–7245. [CrossRef]
75. Pahroraji, M.E.H.M.; Saman, H.M.; Rahmat, M.N.; Kamaruddin, K. Properties of coal ash foamed brick stabilised with hydrated lime-activated ground granulated blastfurnace slag. *Constr. Build. Mater.* **2020**, *235*, 117568. [CrossRef]
76. Wang, J.W.; Nie, X.H.; Lang, L.; Hu, Z.; Chen, B. Recycling electrolytic manganese residue into sustainable subgrade material with carbide slag pretreatment and ground granulated blast-furnace slag stabilization. *Process Saf. Environ. Protect.* **2025**, *203*, 107936. [CrossRef]
77. Wang, H.Y.; Kong, D.W.; Pan, S.Y.; Yang, F.; Xu, F. High-volume phosphogypsum road base materials. *Coatings* **2025**, *15*, 1040. [CrossRef]
78. Yang, D.K.; Kow, K.W.; Meredith, W.; Peng, Y.Q.; Wang, L.; Li, X.; Zhang, G.L.; Zhang, J.Z.; Chen, G.F.; Li, J.W.; et al. Green synthesis of NaP1 zeolite from MSWI fly ash and silica-rich solid waste with superior Cu(II) removal efficiency. *Chem. Eng. J.* **2025**, *522*, 167475. [CrossRef]
79. Zhang, Y.L.; Chao, S.; Zhang, X.; Li, J.G.; Duan, Y.M.; Gu, C.H.; He, J.L. Synthesis and cycling stability mechanism of high temperature calcium-based CO_2 adsorption material $CaO/C_{12}A_7$ from LF refining slag source. *Chem. Eng. J.* **2025**, *505*, 159224. [CrossRef]
80. Shi, X.Z.; Yang, B.G.; Qian, D.Y.; Cui, D.; Li, H.B.; Wang, C.; Zhu, Y.H.; Yu, T. Isotherm, kinetics, and adsorption mechanism studies of coal gasification coarse slag as highly efficient phosphate adsorbents. *Separations* **2024**, *11*, 182. [CrossRef]
81. Wei, Y.; He, L.; Luo, Z.Q.; Zhou, X.T.; Zhang, Z.J.; Luo, Y.L.; Liu, Q. Removal of hexavalent chromium from aqueous solution using low-cost magnetic microspheres derived from alkali-activated iron-rich copper slag. *J. Environ. Chem. Eng.* **2023**, *11*, 110436. [CrossRef]
82. Ning, K.; Zheng, S.C.; He, Y.T.; Hu, Y.; Hao, S.Y.; Cui, Q.L.; Chen, H.S. Removal of fluoride from aqueous solutions through Fe(III) modified water treatment residues. *J. Clean. Prod.* **2023**, *382*, 135374. [CrossRef]
83. Ifthikar, J.; Jiao, X.; Ngambia, A.; Wang, T.; Khan, A.; Jawad, A.; Xue, Q.; Liu, L.; Chen, Z.Q. Facile one-pot synthesis of sustainable carboxymethyl chitosan—Sewage sludge biochar for effective heavy metal chelation and regeneration. *Bioresour. Technol.* **2018**, *262*, 22–31. [CrossRef] [PubMed]
84. Qiu, B.B.; Feng, D.; He, G.S. Value adding industrial solid wastes: Impact of industrial solid wastes upon copper removal performance of synthesized low cost adsorbents. *Energy Sources Part A-Recovery Util. Environ. Eff.* **2020**, *42*, 835–848.
85. Imessaoudene, A.; Cheikh, S.; Hadadi, A.; Hamri, N.; Bollinger, J.C.; Amrane, A.; Tahraoui, H.; Manseri, A.; Mouni, L. Adsorption performance of zeolite for the removal of Congo red dye: Factorial design experiments, kinetic, and equilibrium studies. *Separations* **2023**, *10*, 57. [CrossRef]
86. Guo, Y.X.; Zhang, X.; Xie, Y.S.; Hu, Y.C.; Jia, Z.Q.; Ma, Y.F.; Wang, X. Facile separation of Cu^{2+} from water by novel sandwich NaY zeolite adsorptive membrane. *Separations* **2023**, *10*, 171. [CrossRef]
87. Shakir, K.; Ghoneimy, H.F.; Elkafrawy, A.F.; Beheir, S.G.; Refaat, M. Removal of catechol from aqueous solutions by adsorption onto organophilic-bentonite. *J. Hazard. Mater.* **2008**, *150*, 765–773. [CrossRef]

88. Ibsaine, F.; Azizi, D.; Dionne, J.; Tran, L.H.; Coudert, L.; Pasquier, L.C.; Blais, J.F. Conversion of aluminosilicate residue generated from lithium extraction process to NaX zeolite. *Minerals* **2023**, *13*, 1467. [CrossRef]
89. Lv, Y.W.; Ma, B.Z.; Liu, Y.B.; Wang, C.Y.; Chen, Y.Q. Adsorption behavior and mechanism of mixed heavy metal ions by zeolite adsorbent prepared from lithium leach residue. *Microporous Mesoporous Mater.* **2022**, *329*, 111553. [CrossRef]
90. Sun, Z.H.; Shu, Q.X.; Zhang, Q.K.; Li, S.P.; Zhu, G.Y.; Wang, C.Y.; Zhang, J.B.; Li, H.Q.; Huang, Z.H. A hydrothermal synthesis process of ZSM-5 zeolite for VOCs adsorption using desilication solution. *Separations* **2024**, *11*, 39. [CrossRef]
91. Cheng, Y.; Xu, L.; Liu, C. NaP1 zeolite synthesized via effective extraction of Si and Al from red mud for methylene blue adsorption. *Adv. Powder Technol.* **2021**, *32*, 3904–3914. [CrossRef]
92. Chen, D.; Hu, X.; Shi, L.; Cui, Q.; Wang, H.Y.; Yao, H.Q. Synthesis and characterization of zeolite X from lithium slag. *Appl. Clay Sci.* **2012**, *59–60*, 148–151. [CrossRef]
93. Wang, Z.L.; Luo, X.L.; Zheng, X.J.; Chen, M.; Guo, H.F.; Li, Q. Lithium leach residue synthesis process of high crystallinity hydroxysodalite, NaX, NaA zeolites and solidification and migration of potentially toxic elements. *Arab. J. Chem.* **2024**, *17*, 105871. [CrossRef]
94. Li, C.X.; Zhong, H.; Wang, S.; Xue, J.R.; Zhang, Z.Y. A novel conversion process for waste residue: Synthesis of zeolite from electrolytic manganese residue and its application to the removal of heavy metals. *Colloids Surf. A Physicochem. Eng. Asp.* **2015**, *470*, 258–267. [CrossRef]
95. Kuwahara, Y.; Ohmichi, T.; Mori, K.; Katayama, I.; Yamashita, H. Synthesis of zeolite from steel slag and its application as a support of nano-sized TiO_2 photocatalyst. *J. Mater. Sci.* **2008**, *43*, 2407–2410. [CrossRef]
96. Ameh, A.E.; Fatoba, O.O.; Musyoka, N.M.; Petrik, L.F. Influence of aluminium source on the crystal structure and framework coordination of Al and Si in fly ash-based zeolite NaA. *Powder Technol.* **2017**, *306*, 17–25. [CrossRef]
97. Fukasawa, T.; Karisma, A.D.; Shibata, D.; Huang, A.N.; Fukui, K. Synthesis of zeolite from coal fly ash by microwave hydrothermal treatment with pulverization process. *Adv. Powder Technol.* **2017**, *28*, 798–804. [CrossRef]
98. Bang, J.H.; Lee, S.W.; Jeon, C.; Park, S.; Song, K.; Jo, W.J.; Chae, S. Leaching of metal ions from blast furnace slag by using aqua regia for CO_2 mineralization. *Energies* **2016**, *9*, 996. [CrossRef]
99. Gao, J.M.; Li, Z.; Ma, S.J.; Zhang, Y.Y.; Cheng, F.Q. Novel process for facile preparation of mesoporous silica-based materials with controllable pore structure from coal fly ash. *Particuology* **2024**, *91*, 128–137. [CrossRef]
100. Jankowska, A.; Panek, R.; Franus, W.; Goscianska, J. Fly ash converting into ordered mesoporous silica materials for water purification from azo dyes. *Microporous Mesoporous Mater.* **2025**, *395*, 113683. [CrossRef]
101. Liu, H.N.; Tang, X.C.; Tang, Z.L.; Xiao, Z.Y. A new in situ-formed ferric-aluminum (hydr)oxides prepared by red mud for arsenic removal. *JOM* **2025**, *77*, 3394–3408. [CrossRef]
102. Shon, H.K.; Vigneswaran, S.; Kandasamy, J.; Kim, J.B.; Park, H.J.; Choi, S.W.; Kim, J.H. Preparation of titanium oxide, iron oxide, and aluminium oxide from sludge generated from Ti-salt, Fe-salt and Al-salt flocculation of wastewater. *J. Ind. Eng. Chem.* **2009**, *15*, 719–723. [CrossRef]
103. Chen, H.; Wu, H.N.; Khan, N.S.A.; Peng, X.M.; Qiu, F.X.; Zhang, T. Converting wastes to resource: Preparation of NiO@γ-Al_2O_3 sludge composite from aluminum-containing sludge for cadmium removal from wastewater. *J. Clean. Prod.* **2023**, *392*, 136335. [CrossRef]
104. Abedi, G.; Moghadam, A.J.; Montazeri, A.; Hajyani, Z.; Nezarat, A.; Aghababai Beni, A. Synthesis of green ceramic adsorbent for the treatment of tire factory effluent containing lead, zinc, aluminum, cobalt, iron and manganese ions. *Result Eng.* **2024**, *23*, 102591. [CrossRef]
105. Deng, S.; An, Q.; Ye, Z.H.; Tang, C.Z.; Zhao, B.; Yang, Y.C. Removal of iron and manganese from synthetic acid mine drainage using red mud ceramsite: Synergistic effect of coprecipitation and adsorption. *Colloids Surf. A Physicochem. Eng. Asp.* **2025**, *725*, 137617. [CrossRef]
106. Wu, F.F.; Wang, S.; Guo, S.Y.; Zhong, H. Adsorption of methylene blue by porous ceramics prepared from electrolytic manganese residues. *Desalin. Water Treat.* **2016**, *57*, 27627–27637. [CrossRef]
107. Ma, B.Y.; Su, C.; Ren, X.M.; Gao, Z.; Qian, F.; Yang, W.G.; Liu, G.Q.; Li, H.X.; Yu, J.K.; Zhu, Q. Preparation and properties of porous mullite ceramics with high-closed porosity and high strength from fly ash via reaction synthesis process. *J. Alloys Compd.* **2019**, *803*, 981–991. [CrossRef]
108. Li, Z.J.; Chen, W.J.; Yang, F.H.; Wang, Y.L.; Cui, S.P.; Li, Q.Y.; Nie, Z.R.; Wei, Q. Porous ceramic membranes fabricated mainly from red mud for oily wastewater treatment. *Sep. Purif. Technol.* **2025**, *364*, 132519. [CrossRef]
109. Huang, X.; Luo, Y.; Zhao, X.; Huang, Y.; Wang, X.; Liu, Z. Effect of desulfurized gypsum whiskers on the adsorption performances of red mud-based ceramsites for lead ion. *Int. J. Environ. Sci. Technol.* **2025**, *22*, 6931–6944. [CrossRef]
110. Cusidó, J.A.; Soriano, C. Valorization of pellets from municipal WWTP sludge in lightweight clay ceramics. *Waste Manag.* **2011**, *31*, 1372–1380. [CrossRef]

111. Ma, M.Y.; Ke, X.; Liu, Y.C.; Ha, Z.H.; Wang, T.; Li, J.; Zhang, F.; Zhang, T.C. A novel electrolytic-manganese-residues-and-serpentine-based composite (S-EMR) for enhanced Cd(II) and Pb(II) adsorption in aquatic environment. *Rare Met.* **2023**, *42*, 346–358. [CrossRef]
112. Jiang, J.; Wang, S.F.; Luo, H.H.; Su, J.; Cao, F.S.; Yin, J.; Liu, S.H.; Ou, X.D. Adsorption mechanism of Cd^{2+} on solid waste-based PRB composite filler and pore structure dynamic evolution laws. *J. Clean. Prod.* **2024**, *469*, 143251. [CrossRef]
113. Qi, J.M.; Li, B.; Zhou, P.X.; Su, X.T.; Yang, D.; Wu, J.X.; Wang, Z.X.; Liang, X.J. Study on adsorption of hexavalent chromium by composite material prepared from iron-based solid wastes. *Sci. Rep.* **2023**, *13*, 135. [CrossRef] [PubMed]
114. Feng, D.S.; Yi, J.M.; Liu, Y.X.; Fu, J.Z.; Gong, R.H.; Li, H.D. Efficiency of adsorption of PSNPs using spontaneous magnetic biochar prepared from pyrolysis of municipal sludge and industrial red mud solid waste. *J. Chem. Technol. Biotechnol.* **2025**, *100*, 778–791. [CrossRef]
115. Wei, M.; Wang, B.; Wu, P.; Zhang, X.Y.; Chen, M.; Wang, S.S. Electrolytic manganese residue-biochar composite for simultaneous removal of antimony and arsenic from water: Adsorption performance and mechanisms. *J. Clean. Prod.* **2024**, *437*, 140623. [CrossRef]
116. Liu, J.; Wang, B.; Chen, M.; Wu, P.; Hassan, M.; Zhang, X.Y. Synergistic removal of arsenic and fluoride dual contaminants in water by engineered phosphogypsum-biochar composite: Adsorption behavior and mechanisms. *J. Environ. Chem. Eng.* **2025**, *13*, 118316. [CrossRef]
117. Wang, N.N.; Wang, B.; Zhang, X.Y. TiO_2-loaded phosphogypsum-modified biochar for the removal of ofloxacin and Cu^{2+}: Performance, mechanisms, and toxicity assessment. *Chem. Eng. J.* **2024**, *498*, 155441. [CrossRef]
118. Jiang, Z.H.; Chen, M.; Lee, X.Q.; Feng, Q.W.; Cheng, N.; Zhang, X.Y.; Wang, S.S.; Wang, B. Enhanced removal of sulfonamide antibiotics from water by phosphogypsum modified biochar composite. *J. Environ. Sci.* **2023**, *130*, 174–186. [CrossRef]
119. Li, X.T.; Zhong, W.; Duan, G.Y.; Li, X.Y.; Cai, H.Y.; Wang, S. Spherical red mud-derived NaA zeolite-chitosan composite for enhanced heavy metal removal from wastewater. *J. Environ. Chem. Eng.* **2025**, *13*, 119880. [CrossRef]
120. Li, X.T.; Li, X.Y.; Ma, X.; Li, C.X.; Xue, J.R.; Wang, S. Highly efficient CO_2 mineralization: Mechanisms and feasibility of utilizing electrolytic manganese residue as a feedstock and implementing ammonia recycling. *Sci. Total Environ.* **2024**, *954*, 176711. [CrossRef]
121. Duan, W.J.; Wang, J.H.; Gao, L.H.; Wang, Z.M.; Li, B.W. Unlocking potential of blast furnace slag: CO_2 adsorption performance and mechanism of slag-derived zeolite. *J. Environ. Manag.* **2025**, *393*, 127181. [CrossRef]
122. Duan, G.Y.; Cao, Z.F.; Zhong, H.; Ma, X.; Wang, S. Highly efficient poly(6-acryloylamino-N-hydroxyhexanamide) resin for adsorption of heavy metal ions. *J. Environ. Manag.* **2022**, *308*, 114631. [CrossRef]
123. Fu, F.L.; Wang, Q. Removal of heavy metal ions from wastewaters: A review. *J. Environ. Manag.* **2011**, *92*, 407–418. [CrossRef] [PubMed]
124. Agrawal, A.; Sahu, K.K.; Pandey, B.D. A comparative adsorption study of copper on various industrial solid wastes. *AIChE J.* **2004**, *50*, 2430–2438. [CrossRef]
125. Ibsaine, F.; Dionne, J.; Tran, L.H.; Coudert, L.; Pasquier, L.C.; Blais, J.F. Application of aluminosilicate residue-based zeolite from lithium extraction in water treatment. *Microporous Mesoporous Mater.* **2025**, *381*, 113370. [CrossRef]
126. Xu, Y.Z.; Qing, Y.J.; Gu, R.M.; Zhou, S.; Fu, G.Y.; Zhao, Y.Y. Efficient adsorption of Tl(I) from aqueous solutions using Al and Fe-based water treatment residuals. *Processes* **2022**, *10*, 2700. [CrossRef]
127. Ge, S.Y.; Zhang, H.; Ye, H.; Zhang, H.H.; Zhao, K.Q.; Sun, Q.F.; Wu, R.; Cao, W.P. Sorption behavior of phosphate on an MSWI bottom slag and sewage sludge co-sintered adsorbent. *Water Air Soil Pollut.* **2013**, *224*, 1683. [CrossRef]
128. Sousa, D.; Bernardo, M.; Matos, I.; Fonseca, I.; Dias, R.; Maurício, R. Key properties of drinking water treatment residuals for their effective reuse as phosphate adsorbents. *Environ. Process.* **2025**, *12*, 39. [CrossRef]
129. Xie, D.A.; Sun, Y.; Yang, Y.L.; Shi, X.L.; Suo, G.Q.; Hou, X.J.; Ye, X.H.; Zhang, L.; Chen, Z.G. Remarkable purification of organic dyes by NiOOH-modified industrial waste residues. *J. Colloid Interface Sci.* **2024**, *664*, 136–145. [CrossRef]
130. An, D.D.; Sun, Y.; Yang, Y.L.; Shi, X.L.; Chen, H.J.; Zhang, L.; Suo, G.Q.; Hou, X.J.; Ye, X.H.; Lu, S.Y.; et al. A strategy-purifying wastewater with waste materials: Zn^{2+} modified waste red mud as recoverable adsorbents with an enhanced removal capacity of Congo red. *J. Colloid Interface Sci.* **2023**, *645*, 694–704. [CrossRef]
131. Zhang, Z.M.; Sarkar, D.; Datta, R.; Deng, Y. Adsorption of perfluorooctanoic acid (PFOA) and perfluorooctanesulfonic acid (PFOS) by aluminum-based drinking water treatment residuals. *J. Hazard. Mater. Lett.* **2021**, *2*, 100034. [CrossRef]
132. Sousa, D.; Bernardo, M.; Sellaoui, L.; Bonilla Petriciolet, A.; Mokhati, A.; Mauricio, R. Reuse of drinking water treatment sludge for the removal of antibiotics: The case study of sulfamethoxazole and trimethoprim based on advanced statistical physics models. *J. Hazard. Mater. Adv.* **2025**, *18*, 100737. [CrossRef]
133. Apeksha, M.; Rajanikanth, B.S. Plasma/adsorbent system for NO_x treatment in diesel exhaust: A case study on solid industrial wastes. *Int. J. Environ. Sci. Technol.* **2019**, *16*, 2973–2988. [CrossRef]
134. Fotsop, C.G.; Lieb, A.; Scheffler, F. Insights into the synergistic effects of ZnO/MgO and Zn/Mg-modified porous zeolite as core-satellite materials for tuning water vapor sorption properties. *Appl. Surf. Sci. Adv.* **2025**, *30*, 100855. [CrossRef]

135. Fotsop, C.G.; Lieb, A.; Scheffler, F. Core-satellite material based metal-doped zeolite LTA for highly efficient iodine sequestration: Adsorption performance and mechanism. *Inorg. Chem. Commun.* **2026**, *183*, 115742. [CrossRef]
136. Liang, W.J.; Zhang, Y.; Yang, L.; Liu, J. Adsorption performance of amine-functionalized red mud-based adsorbent for CO_2 capture. *J. Environ. Manag.* **2025**, *383*, 125334. [CrossRef] [PubMed]
137. Li, Y.C.; Chen, Z.; Yuan, B.L.; Xing, L.; Zhan, G.X.; Peng, Y.; Wang, L.D.; Li, J.H. Synergistic promotion for CO_2 absorption and solvent regeneration by fine waste red mud particles on in amine-based carbon capture: Performance and mechanism. *Sep. Purif. Technol.* **2023**, *304*, 122380. [CrossRef]
138. Xu, Z.; Lu, Z.; Zhang, L.; Fan, H.; Wang, Y.; Li, J.; Lin, Y.; Liu, H.; Guo, S.; Xu, M.; et al. Red mud based passivator reduced Cd accumulation in edible amaranth by influencing root organic matter metabolism and soil aggregate distribution. *Environ. Pollut.* **2021**, *275*, 116543. [CrossRef]
139. Chen, T.; Wang, L.H.; He, B.; Peng, X.C.; Nie, X.Q.; Ma, F.L.; Han, P.J.; Bai, X.H. Study on the solidification/stabilization of cadmium-contaminated soil by red mud-assisted blast furnace slag under excitation conditions. *J. Clean. Prod.* **2024**, *435*, 140505. [CrossRef]
140. Wei, M.; Wang, B.; Chen, M.; Wu, P.; Zhang, X.Y. Remediation of antimony and arsenic in co-contaminated soil by electrolytic manganese residue-biochar composite: Effects, mechanisms, and microbial response. *Environ. Pollut.* **2025**, *366*, 125371. [CrossRef]
141. Wang, S.; Zhong, H.; Liu, G.Y.; Zhang, Q.; Li, T. Synthesis and adsorption properties for Au(III) of alkoxycarbonyl thiourea resin. *J. Cent. South Univ. Technol.* **2008**, *15*, 463–468. [CrossRef]
142. Han, M.Y.; Shen, X.Y.; Guo, J.Q.; Liu, Y.; Zhai, Y.C. Green synthesis pathway: Transforming industrial waste into high-performance MgAl-LDO adsorbent and the innovative applications in heavy metal ions capture. *J. Water Process Eng.* **2025**, *73*, 107704. [CrossRef]
143. Chen, L.X.; Zuo, Q.; Zhang, Q.W.; He, X.M. Low temperature synthesis of carbon-based adsorbents from cellulose or biomass solid waste and its evaluation of cadmium ions removal from water. *Mater. Today Commun.* **2025**, *42*, 111174. [CrossRef]
144. Gao, S.J.; Wang, C.H.; Pei, Y.S. Comparison of different phosphate species adsorption by ferric and alum water treatment residuals. *J. Environ. Sci.* **2013**, *25*, 986–992. [CrossRef]
145. Zhou, X.T.; Li, L.J.; Qiu, Y.Q.; Liu, W.S. Adsorption of phosphate by cancrinite in red mud: A first-principles study. *Mater. Res. Express* **2022**, *9*, 045503. [CrossRef]
146. Abadee, Z.G.N.; Hekmati, M.; Ganji, M.D. Removing phenol contaminants from wastewater using graphene nanobuds: DFT and reactive MD simulation investigations. *J. Mol. Liq.* **2019**, *286*, 110872. [CrossRef]
147. Zhou, K.; Ma, W.W.; Zeng, Z.; Chen, R.F.; Xu, X.; Liu, B.G.; Li, H.L.; Li, H.Y.; Li, L.Q. Waste biomass-derived oxygen and nitrogen co-doped porous carbon/MgO composites as superior acetone adsorbent: Experimental and DFT study on the adsorption behavior. *Chem. Eng. J.* **2020**, *387*, 124173. [CrossRef]
148. Wei, D.L.; Zhao, C.F.; Khan, A.; Sun, L.; Ji, Y.F.; Ai, Y.J.; Wang, X.K. Sorption mechanism and dynamic behavior of graphene oxide as an effective adsorbent for the removal of chlorophenol based environmental-hormones: A DFT and MD simulation study. *Chem. Eng. J.* **2019**, *375*, 121964. [CrossRef]
149. Huang, M.M.; Tan, J.; Xia, L.Y.; Han, K.; Cai, H.; Ma, X.; Wang, S. A comprehensive review of adsorbents for rare earth separation: Design, synthesis, adsorption performance, and mechanisms. *Rare Met.* **2026**, *45*, e70056. [CrossRef]

Disclaimer/Publisher's Note: The statements, opinions and data contained in all publications are solely those of the individual author(s) and contributor(s) and not of MDPI and/or the editor(s). MDPI and/or the editor(s) disclaim responsibility for any injury to people or property resulting from any ideas, methods, instructions or products referred to in the content.